공학석사학위논문

Characteristics of Hybrid Process Using Dry Nanoparticle Deposition and Micromachining

건식 나노입자 적층과 마이크로머시닝을 이용한 하이브리드 가공 특성

2016 년 2 월

서울대학교 대학원

기계항공공학부

김 은 섭

Characteristics of Hybrid Process Using Dry Nanoparticle Deposition and Micromachining

건식 나노입자 적층과 마이크로머시닝을 이용한
하이브리드 가공 특성

지도교수 안 성 훈

이 논문을 공학석사 학위논문으로 제출함
2015 년 10 월

서울대학교 대학원
기계항공공학부
김 은 섭

김은섭의 공학석사 학위논문을 인준함

2015 년 12 월

위 원 장 박 희 재 (인)

부위원장 안 성 훈 (인)

위 원 차 석 원 (인)

Abstract

Characteristics of Hybrid Process Using Dry Nanoparticle Deposition and Micromachining

Eunseob Kim

Department of Mechanical and Aerospace Engineering

The Graduate School

Seoul National University

With advances in technology and increasing customer demands, developers of commercial products and devices are pursuing properties such as multi-functionality, compact size, and high reliability to improve manufacturing and processing technologies. Microscale and nanoscale manufacturing processes and technologies are increasingly being used in various fields. However, the use of a single manufacturing process generally involves inherent drawbacks, such as limitations in size, material, geometry, and quality. To overcome these limitations, two or more manufacturing processes are often combined in a hybrid manufacturing process.

This dissertation presents two different microscale processes that were integrated for use in a microscale hybrid process involving additive and subtractive process. The additive process was an aerodynamically focused nanoparticle (AFN) printing system, which is a novel process of dry nanoparticle deposition. The subtractive process was mechanical micromachining. These two processes were incorporated into one platform.

The deposition and adhesion characteristics of nanoparticles were investigated with regard to deposition shape and pattern. Deposition performance was evaluated based on adhesion measurement. Shear adhesion strength was quantitatively measured and surface morphologies of deposited nanoscale features were

investigated using scanning electron microscopy (SEM).

For micromachining, the machining plane was defined using the four-point contact method. A tungsten carbide micro-tool with multi-helical edges was fabricated using a focused ion beam (FIB) Micromachining strategies for face milling of the microstructure and slot milling of the conductive line were developed and valuated. After the hybrid process was complete, the mechanical properties of the silver microstructure were valuated using nanoindentation.

The AFN printing process successfully fabricated a superhydrophobic surface with various lattice patterns. An anisotropic hydrophobic surface was fabricated using microgroove patterns. This hybrid process makes it possible to control the surface contact angle passively. These results can be applied to improve manufacturing technologies, by combining different manufacturing processes.

Keyword ： Hybrid process, Aerodynamically focused nanoparticle printing, Mechanical micromachining, Hydrophobic surface

Student Number：2013-20656

Contents

Table of Contents

List of Tables

List of Figures

Chapter 1. Introduction

1.1. Study Background

With advances in technology and increasing customer demands, developers of commercial products and devices are pursuing properties such as multi-functionality, compact size, and high reliability to improve manufacturing and processing technologies. Microscale and nanoscale manufacturing processes and technologies are increasingly being used in industrial, medical, military, and academic applications [1, 2]. Many studies have demonstrated the feasibility of transforming conventional macroscale manufacturing into microscale and nanoscale manufacturing [3].

Although various microscale and nanoscale manufacturing processes are used in manufacturing, such as micromachining, additive manufacturing, welding, chemical etching, etc., each single process has inherent drawbacks such as limitations in size, material, geometry, and quality [2-4]. For example, the micromachining process has limitations in terms of the geometry of final products, and accessibility to the workpiece is restricted. Although additive manufacturing processes, typically fused deposition modeling (FDM), can fabricate full three-dimensional (3D) shapes, they also result in poor surface properties, such as the stair-step effect, and dimensional error due to the liquefied effect [5, 6]. To overcome these limitations, two or more manufacturing processes may be combined to form a hybrid manufacturing process [4, 7]. Researchers are exploring ways to apply hybrid manufacturing processes for microscale and nanoscale fabrication [8]. However, much more work is needed to clarify material behaviors at the microscale and nanoscale, the process capabilities of certain manufacturing processes, and even the operational philosophy behind manufacturing [9]. Figure 1.1 presents various microscale and nanoscale manufacturing processes that have been developed previously [10, 11].

Ahn's research group at Seoul National University developed a nanoscale hybrid 3D printing system that can be used to fabricate nanoscale and microscale prototypes using various materials including ceramics and metals [8, 11-13]. The nanoscale 3D printing system is a novel process technique using a focused ion beam (FIB), nanoparticle deposition system (NPDS), and a local planarization process [8, 12].

Although the system produces successful results, the components have not been fully integrated into one platform [8]. Additionally, the strategies for each additive or subtractive component of the hybrid process are still insufficient, as is knowledge about their mechanisms. More research on microscale hybrid processes is required to improve performance and overcome drawbacks.

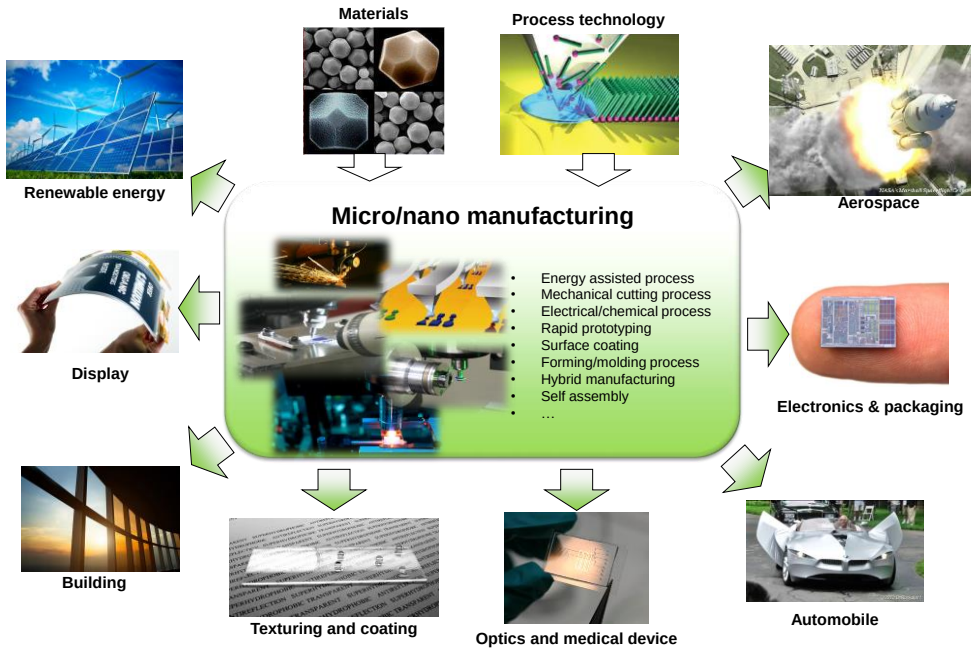

Figure 1.1. Microscale and nanoscale manufacturing technologies and their applications

1.2. Purpose of Research

This dissertation presents two different microscale processes that were integrated for use in a microscale hybrid process involving additive and subtractive processes. The additive process was an aerodynamically focused nanoparticle (AFN) printing system, which is a novel process of dry nanoparticle deposition. The subtractive process was mechanical micromachining. These two processes were incorporated into one platform, and the characteristics of the hybrid process were investigated for various applications. Figure 1.2 presents a schematic of the integrated hybrid process with the additive and subtractive processes.

The deposition and adhesion characteristics of nanoparticles were investigated with regard to deposition shape and patterns. Deposition performance was evaluated based on adhesion measurements. Shear adhesion strength was quantitatively measured and surface morphologies of deposited nanoscale features were investigated using scanning electron microscopy (SEM).

For micromachining, the machining plane was defined using the four-point contact method for calibrating tilted substrate. A tungsten carbide micro-tool with multi-helical edges was fabricated using an FIB. Micromachining strategies for face milling of the microstructure and slot milling of the conductive line were developed and evaluated. After the hybrid process was complete, the results were investigated using SEM images and a confocal microscopy, and the mechanical properties of the silver microstructure were evaluated using nanoindentation.

Additionally, one characteristic of the hybrid process, the surface contact angle, was measured and analyzed based on AFN printing and planarization. Anisotropic surface contact angles were investigated for different AFN printing pattern parameters.

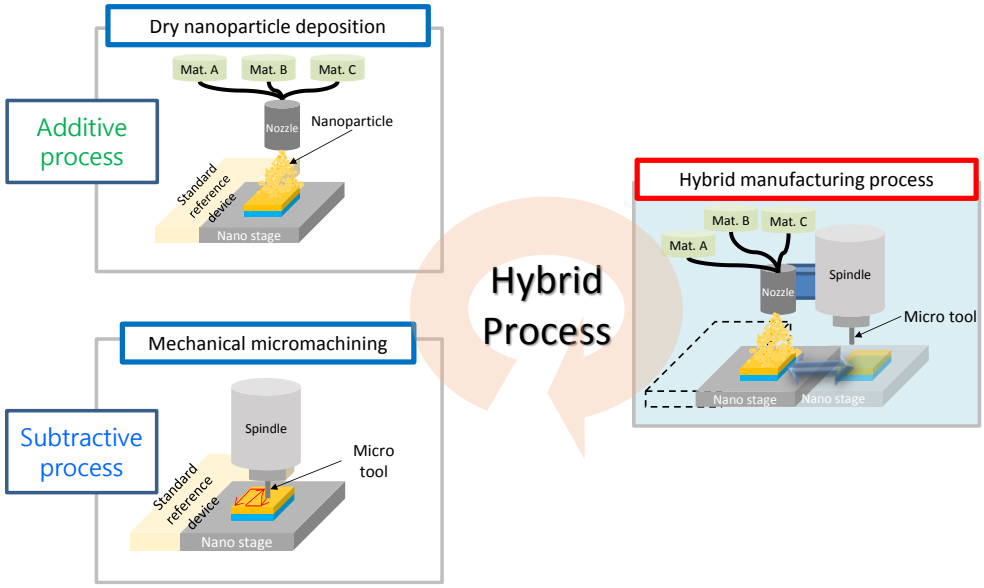

Figure 1.2. Schematic of the hybrid process incorporating dry nanoparticle deposition and mechanical micromachining

Chapter 2. Hybrid process

2.1. Overview

Research about hybrid manufacturing has become more important for industrial and academic applications. Over the past two decades, many hybrid processes have been developed to exploit synergistic effects between two or more different processes [4]. Hybrid manufacturing combines processes or machines to produce parts in a more efficient and productive way [14]. Hybrid manufacturing technologies can process materials or shapes that could not be processed previously, and can also reduce processing costs. In the field of manufacturing technology, the term ‘hybrid’ is often used to refer to processes that combine several kind of technologies [7].

To overcome the disadvantages of each additive and subtractive process, two or more manufacturing processes may be combined to form a hybrid manufacturing process, exploiting the advantages of one process and overcoming the limitations of another [4, 14]. Hybrid processes can be classified in many ways, such as by their combinations of different energy sources and controlled applications of process mechanisms [14]. Zhu et al. reviewed hybrid manufacturing and combined processes, and classified them based on their type of process mechanism: additive and subtractive processes; subtractive and joining processes; additive and transformative processes; and subtractive and transformative processes Chu et al. reviewed 57 microscale and nanoscale hybrid processes, and classified the processes by their timing and type; machining was the most frequently used microscale hybrid process [4]. Chu et al. also reviewed main to main (M/M) sequence hybrid processes (nanoscale and microscale) and considered ways to overcome the limitations of each single process.

In this chapter, M/M sequence hybrid processes was reviewed from nanoscale to microscale and considered in order to overcoming limitations of each single process. Assisted and mixing mechanism processes were not considered. M/M sequence hybrid manufacturing processes means that those consist only of additive and/or subtractive processes, without an assistive process [4].

2.2. Review of hybrid process

Combining additive and subtractive processes in sequence can yield synergistic effects, which can overcome limitations related to precision, geometry, and material. Additive and subtractive processes can be used to fabricate parts with complicated geometries, and functional parts with functional multi-materials. This section reviews M/M sequence processes at the microscale and nanoscale level.

Hybrid processes including additive and subtractive M/M sequence processes have used since the early 1990s. In 1991, Carnegie Mellon University reported a hybrid mask and deposition (MD) system for solid freeform fabrication, using masking, thermal spray shape deposition, and milling to ensure accurate shapes [15]. Stanford University reported a shape deposition manufacturing (SDM) system based on combinations of additive and subtractive processes [16]. SDM can fabricate shapes using not only metal and ceramic, but also polymers including wax. SDM can be used for applications including biologically inspired microstructures [17] and functional gradient metallic prototypes [18]. Seoul National University and INUS Technology, Inc. (Seoul, Korea) reported ECLIPSE-RP, which is an additive and subtractive sequence process for achieving high accuracy at the macroscale level [19, 20]. A nano composite deposition system (NCDS) was developed by integrating fused deposition and micromachining processes from the microscale to the macroscale [21].

NEC Fundamental Research Laboratories (Tsukuba, Japan) reported a nanoscale hybrid process using a FIB and chemical vapor deposition (CVD) [22]. This FIB-CVD hybrid process can fabricate 3D shapes at sub-microscale levels under high vacuum conditions. It has been used in applications such as producing nano-tweezers using shape memory alloy (SMA) and Pt, which can be actuated by thermal energy [23]. The University of Hyogo and CREST JST (Saitama, Japan) reported a nanoscale hybrid process using an electron beam (EB) and CVD [24]. In 2011, Ahn's research group at Seoul National University developed a nanoscale hybrid 3D printing system consisting initially of NPDS and FIB [11, 13]. Nanoscale hybrid 3D printing systems have been improved by using AFN printing as a substitute for NPDS, and using local planarization processes based on dry mechanical grinding [8, 12]. Nanoscale hybrid 3D printing systems can achieve a feature size of 300 nm and

an accuracy of 50 nm [8]. However, most nanoscale hybrid 3D printing systems have as many platforms as processes. Sequence processes that operate in one platform provide several advantages, including reduced process time and improved precision [7, 20, 21].

Figure 2.1 presents the scale of feature size by year of development. Some hybrid processes (nanoscale to microscale) can be conducted under vacuum conditions, but others need atmospheric pressure conditions. These different operating conditions can make it difficult to integrate the processes into one platform.

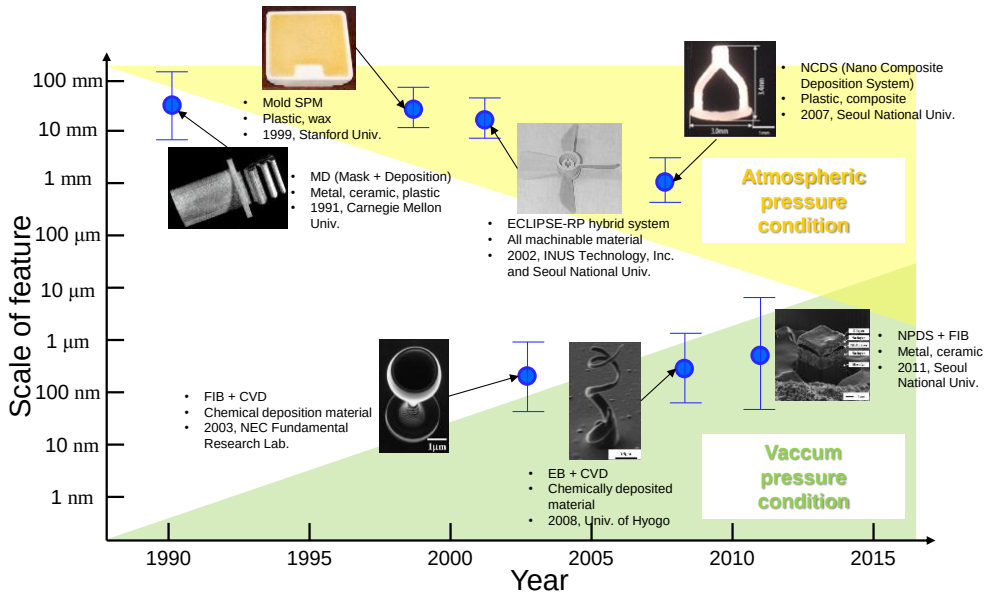

Figure 2.1. Scale of feature size by year of hybrid process development, using main to main (M/M) sequences for available multi-materials

2.2. System configurations

Dry nanoparticle deposition process as an additive process and mechanical micromachining as a subtractive process were integrated in a platform for improving precision, complicated geometry and quality. The advantage of integrated system includes positioning error of the process because it is possible to sharing coordinates [20]. However operating conditions of each process are different. Although mechanical micromachining is required for atmospheric condition, dry nanoparticle deposition process is required for vacuum condition in order to accelerate nanoparticle for deposition [10, 25, 26]. If the chamber for making vacuum condition over the whole system including mechanical micromachining part, the cost of an equipment would be much high. Therefore mini chamber which can be moved from top to bottom repeatedly was used for a dry nanoparticle deposition part. When dry nanoparticle process operates, the mini vacuum chamber comes down to the plate on the top of the stage system. Then vacuum chamber and the plate are compacted by clamping tool. For movement of the 3-axis at the clamping state, a flexible metal bellow was used. The available travel as compacted up for dry nanoparticle deposition process was 100 mm for all of the direction including the x, y, and z axis. Then mechanical micromachining process operates, the mini vacuum chamber goes up to initial position and is hooked up for prevention of deflection of the chamber because of self-weight and flexible bellows.

Hardware configurations of hybrid process which consists of dry nanoparticle deposition and mechanical micromachining are shown in Figure 2.2 and Figure 2.3, respectively. Figure 2.4 shows schematic diagram of integrated hybrid system. Transfer and manipulation, the x, y and z axis stage (JL 200LM (the x and y axis), JHZ-12X (the z axis), JCT Inc., Republic of Korea) was equipped. In the dry nanoparticle deposition system, aerosol generator (RBG 1000, Palsa GmbH, Germany) was used in order to feeding nanoparticles and vacuum pump was equipped for making vacuum condition in the chamber. Nozzle connector was equipped with the exchangeable connector. In mechanical micromachining, air bearing turbine spindle (D1733, WestWind Inc., UK) was equipped. The maximum speed of the spindle is 250,000 rpm. For observing machining process and contact of milling tool, two vision systems were installed (Figure 2.3).

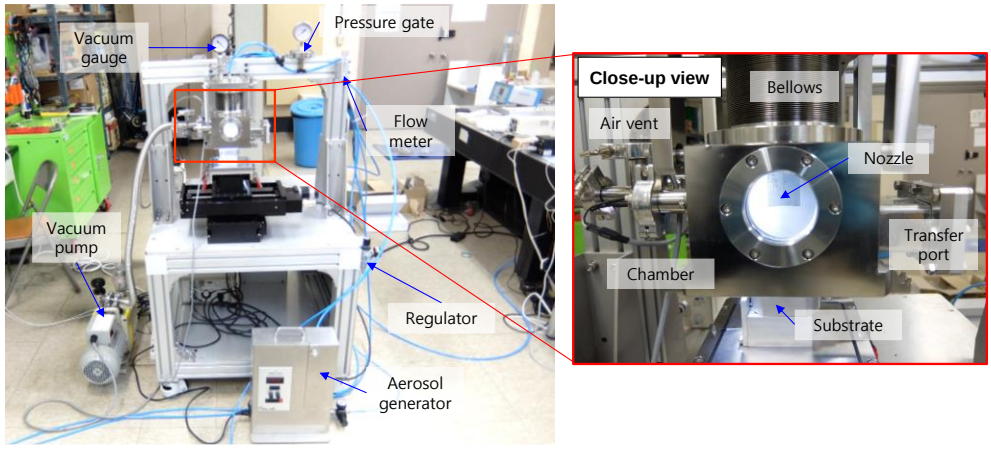

Figure 2.2. Hardware configurations of dry nanoparticle deposition part

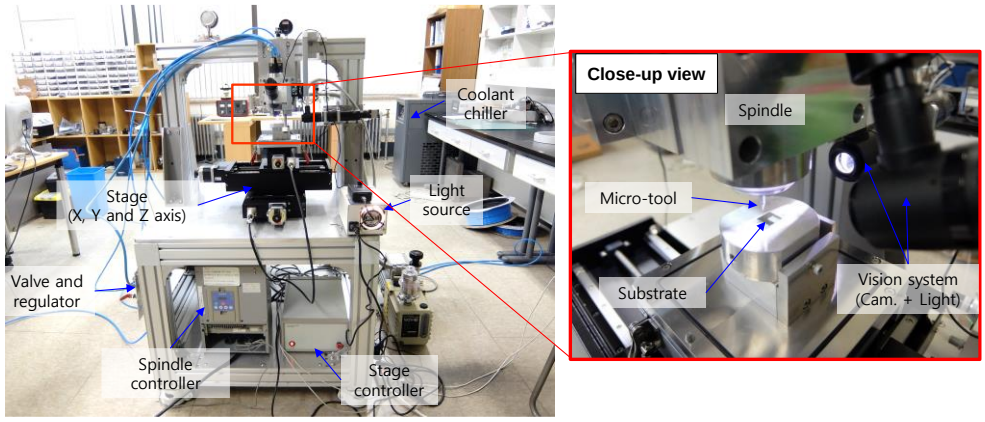

Figure 2.3. Hardware configurations of mechanical micromachining part

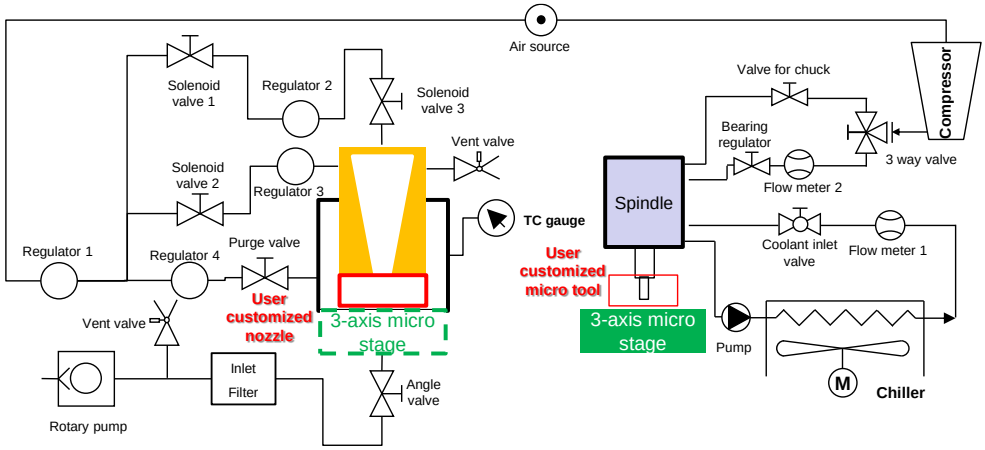

Figure 2.4. A schematic diagram of the hybrid process system

Chapter 3. Dry nanoparticle deposition

3.1. AFN printing

Direct writing technology is one of the main categories of manufacturing technologies. It is additive manufacturing technology to deposit particle without any other masks [27-29]. Dry nanoparticle deposition systems including cold spray, NPDS, and aerosol deposition method are widely used for not only fabrication of microscale prototypes and patterning, but also energy harvesting devices [30-32].

AFN printing was mainly considered in this hybrid process as an additive process because it shows more superior performance than NPDS in terms of micro patterning, manipulating, and micro scale width feature size [25]. AFN printing can be used for direct printing of the solvent-free and inorganic nanoparticles. Schematic diagram of AFN printing system is shown in Figure 3.1. The fast excitation-purge control technique was proposed and investigated by examining the patterning examples [10, 25]. Figure 3.2 shows an example of the fast excitation-purge control technique [10]. Sequence control of purge and flow control valve enables it can deposit nanoparticles smaller size than diameter of nozzle exit [25]. In addition, AFN printing can fabricate variable patterns using ceramics and metals as well.

Performances of NPDS and AFN printing were qualitatively evaluated by various ways such as surface profiles, optical view, and based on deposition height [10, 26, 33, 34]. Table 3.1 shows deposition quantitative compatibility of NPDS and AFN printing of representative materials [8, 10, 33]. However evaluation of deposition performance was insufficient in terms of the performance and the efficiency of deposition. Also deposition mechanical properties like toughness and strength are important issues in additive process using variable material [35, 36]. In addition, aerodynamically focusing effect of AFN printing enables deposition in a tens of micrometer size of feature.

In this chapter, deposition characteristics of dot deposition and conductive line deposition of silver (Ag) nanoparticle using AFN printing was investigated in terms of microstructure and surface morphology in nanoscale. For evaluation of deposition performance, adhesion tests were suggested and evaluated to silver nanoparticle on silicon wafer substrate.

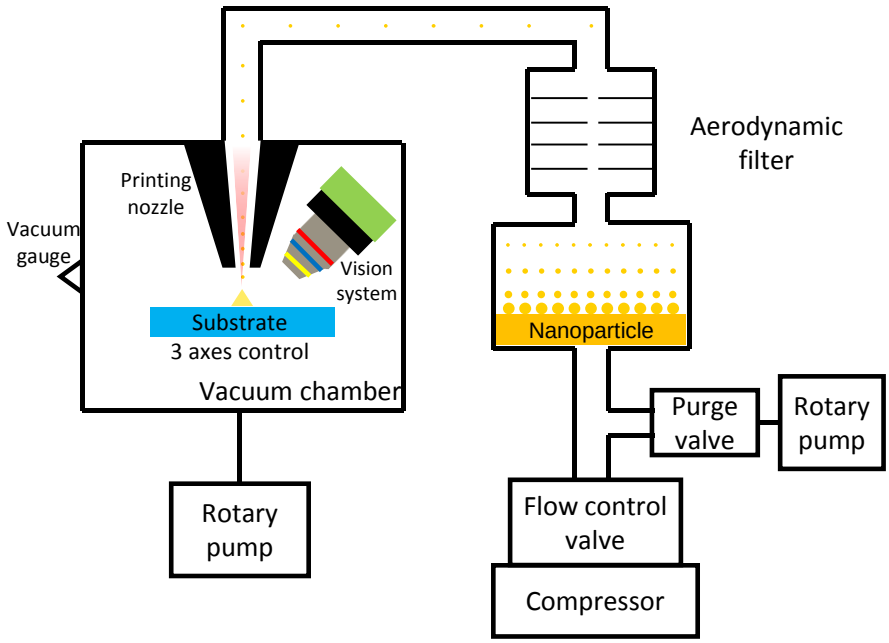

Figure 3.1. Schematic of AFN printing system

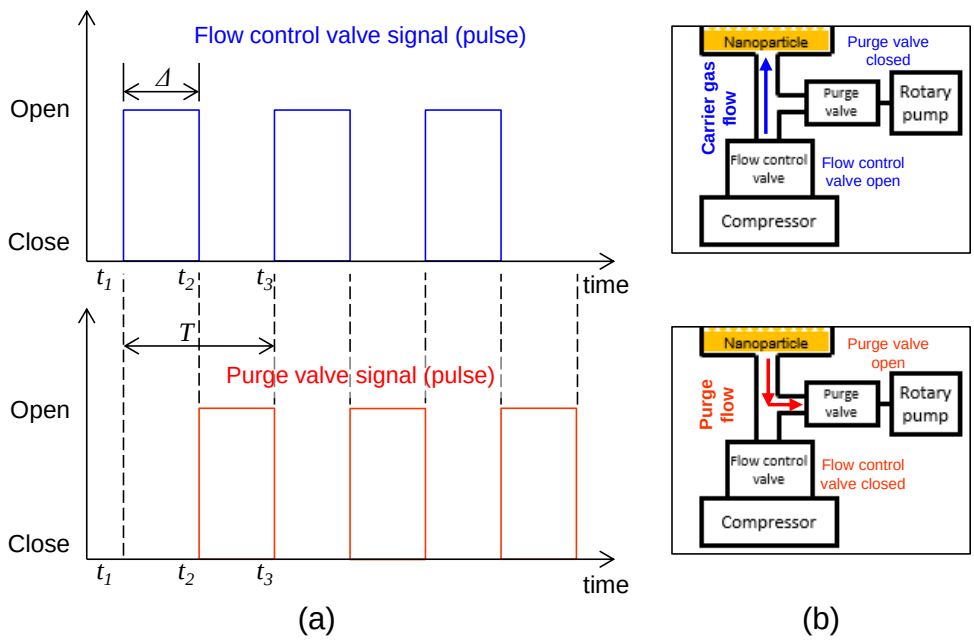

Figure 3.2. The fast excitation-purge control technique; (a) the example of timing diagram of valves opening and closing sequence and (b) the schematic figure depicts carrier gas and purge gas flow directions [10]

Table 3.1. Deposition compatibility of NPDS and AFN printing [8, 10, 33]

Particle \ Substrate		Polymers				Metals			Ceramics		
		PET	PP	PE	PMMA	Cu	Ni	Al	Si	Al_2O_3	Glass
Ceramics	TiO_2	(O)/O*	(△)	(△)	(O)/△*	O	(O)	O	O/△*		O/△*
	Al_2O_3					(O)		(O)	(X)	O	O
	$BaTiO_3$	□*							O*		O*
Metals	Ag	O*			O*				O*		
	Sn	O			O	(O)	O	(O)	O		O
	Cu										
	Al		(O)							(O)	
	Ni	(△)		(△)	(△)				(X)		(X)

Red symbol: NPDS
Blue symbol*: AFN printing
X: No deposition
△: Particle attachment (not film)
□: Deposition with specific condition
O: Well deposition
( ) means that the result was judged by optical images without SEM, surface profile, cross-section result

3.2. Deposition characteristics

3.2.1. Experimental detail

AFN printing can fabricate a single conical-cone shape microstructure using dot deposition and micro line. Silver nanoparticle under 100 nm diameter (Ag 576832-5G, Sigma Aldrich, USA) was used for fabrication of micro structure and conductive line deposition. A metal converging nozzle exit diameter is 500 μm was used for deposition. Because of focused aerosol flow, the size of structure could be fabricated by smaller than nozzle diameter [25]. Silicon wafer was used for substrate of AFN printing.

Table 3.2 shows process parameters of AFN printing for fabricating dot and line deposition and patterning. All of parameters including source pressure (P_s), chamber pressure (P_c) and sampling period (T) were decided for depositing smaller structures based on contour of particle deposition criteria [25]. Stand-off distance (SOD) means the distance from substrate to end of nozzle exit. Deposition size could be controlled by holding time and feed rate parameters. In case of short holding time, fabricated microstructure for dot deposition is smaller than long holding time. In line deposition, small feed rate affect thin line width in line deposition. More than 50 dot deposition samples were fabricated and investigated.

Figure 3.3 shows an example of dot deposition result of silver nanoparticle fabricated by AFN printing on the silicon wafer substrate. Reference mark for measuring height of the microstructure was fabricated by FIB with 30 μm length and 1 μm width (Figure 3.3. (a)). D means diameter of microstructure and H^* means distance between the reference mark and top of microstructure. From SEM images with reference mark, height and diameter could be measured.

Table 3.2. Process parameters of AFN printing

Parameter	Value	Unit
Stand-off distance, *SOD*	1	mm
Source pressure, P_s	200	kPa
Chamber pressure, P_c	0.1	kPa
Sampling period, T	300	msec
Time duration, Δ	150	msec
Holding time*	0.5 - 1	sec
Feed rate**	0.5 - 1	μm/s
Carrier gas	Air	-
Nanoparticle material	Ag	-
Substrate material	Silicon wafer	-

* Dot deposition
** Line deposition

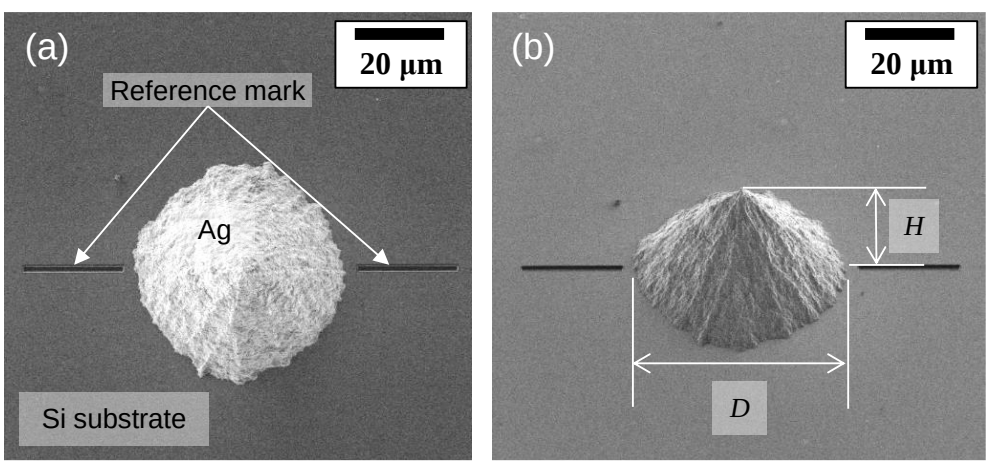

Figure 3.3. Scanning electron microscopy (SEM) images of dot deposition of silver microstructure fabricated by AFN printing on silicon wafer substrate; (a) front view with reference mark, (b) 45° tilt view with deposition parameters

3.2.1. Deposition shape and surface quality analysis

As one of the deposition characteristics of dot deposition using AFN printing, deposition shape and ratio of diameter and height of microstructure was investigated. Figure 3.4 shows an example of line width 150 μm of silver conductive line deposition result. In line deposition result, cross section of conductive line was triangle shape. In conductive line deposition of silver nanoparticle, available line width was from minimum 30 μm to 100s μm. The line width could be controlled by using control of the feed rate parameter.

Parameters of deposition shape were shown in Figure 3.3. (b). Height of microstructure (H) was calculated by $H^{*}\times\sin 45^{\circ}$ because of the angle of tilted images was 45°. Diameter versus height of the microstructure is shown in Figure 3.5. The result showed that increasing rate of ratio of diameter and height was nonlinear because of aerodynamically focusing effect and drag of carrier gas cause it. Simulation of particle deposition of AFN printing was analyzed by using smoothed particle hydrodynamics (SPH) [37]. The simulation predicted similar result with this experimental result. This experimental result is expected to contribute to further analysis of deposition mechanism and principle.

Figure 3.6 shows high magnification image of silver nanoparticle in raw condition. Whereas Figure 3.7 shows the surface morphology of fabricated silver microstructure. The right images of each figures have same magnification. The result shows that silver nanoparticles are agglomerated after deposition but single nanoparticles seemed much smaller than raw condition. Figure 3.8 shows results of image processing from the results from images of Figure 3.6 and Figure 3.7. Open source Image J was used for image processing. Single nanoparticles were tracked by band pass filter and single-band threshold method with circularity of nanoparticle ranged from 0.6 to 1. The average of nanoparticles was 24.8 nm and 25.4 nm in the raw condition (Figure 3.8. (a)) and after deposition (Figure 3.8.(b)), respectively. The standard deviation of the results was 25.8 nm and 18.3 nm in the raw condition and after deposition, respectively. Although average value was similar each other, standard the value of standard deviation different. The result shows size of silver nanoparticles in raw condition has wide distribution compared with the nanoparticles after deposition. It seems that nanoparticles are filtered pass through aerodynamic filter.

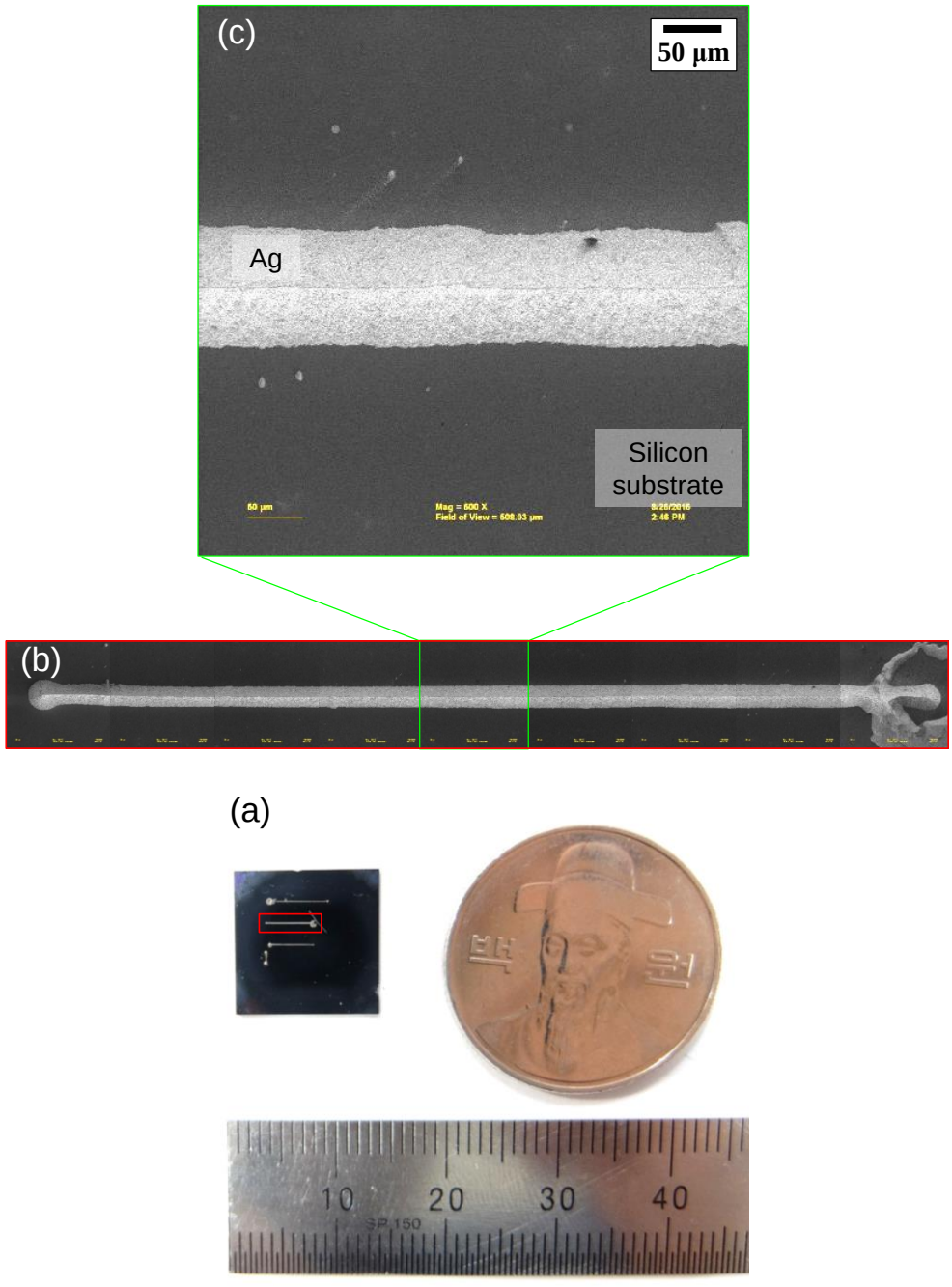

Figure 3.4. An example of silver conductive line deposition fabricated by AFN printing on silicon wafer substrate; (a) a comparison of scale, (b) a SEM image of the whole silver conductive line (boxed area in (a)), and (c) a magnified SEM image

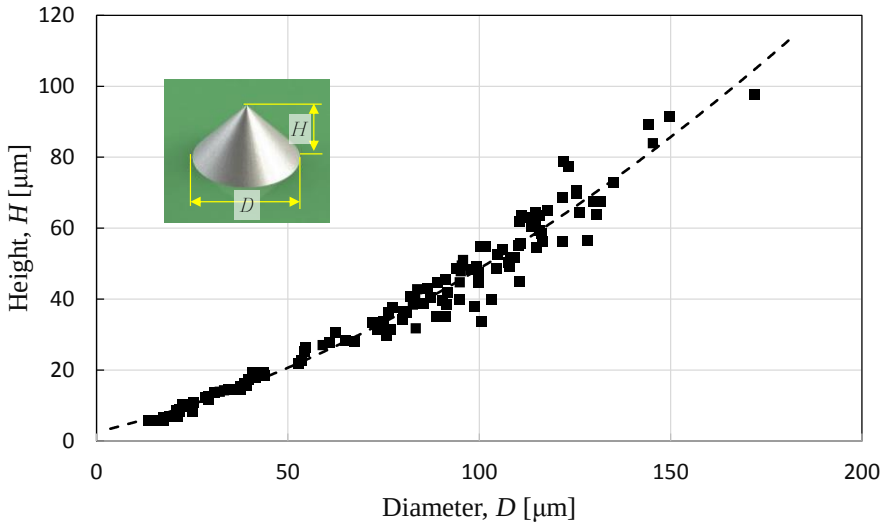

Figure 3.5. Diameter versus height of silver microstructure of dot deposition

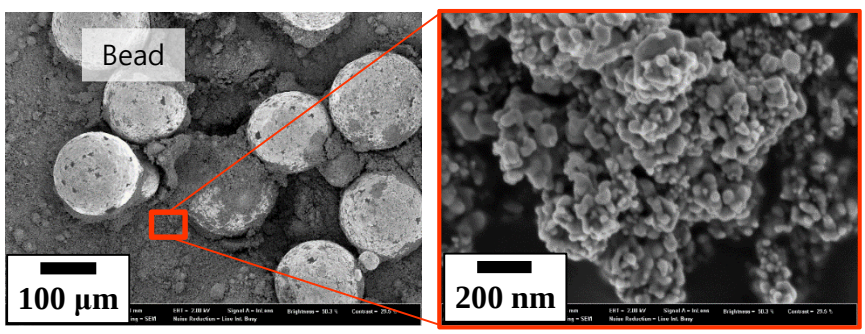

Figure 3.6. SEM image of silver nanoparticles at the raw condition

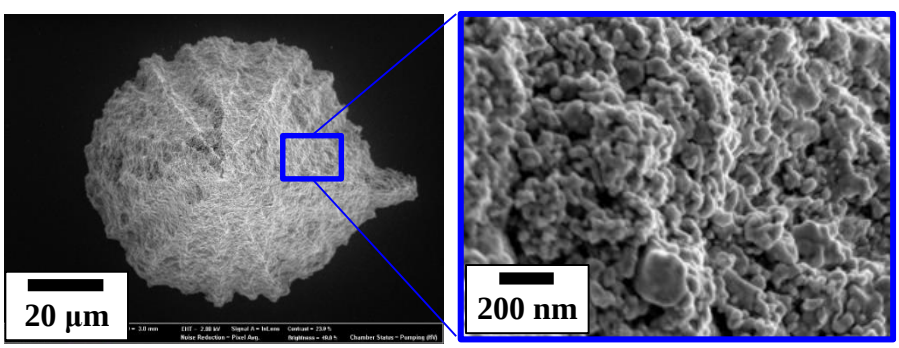

Figure 3.7. SEM image of silver microstructure after deposition with surface morphology

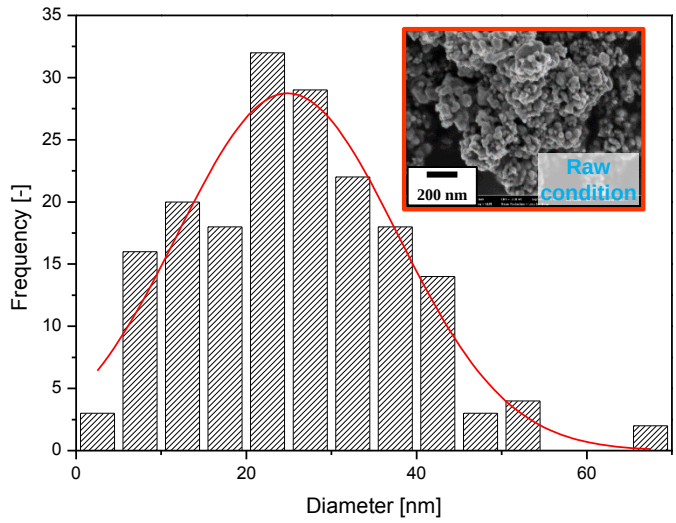

(a)

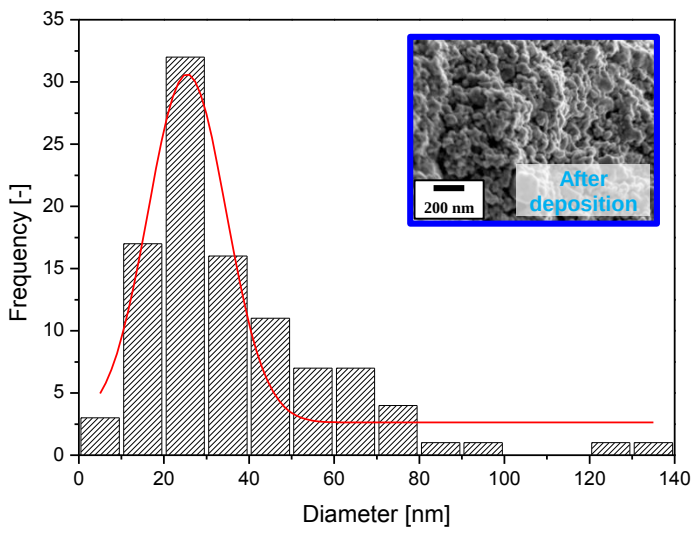

(b)

Figure 3.8. Silver nanoparticle size distributions with Gaussian curves using image processing; (a) raw condition and (b) surface after deposition

3.3. Adhesion characteristics

3.3.1. Adhesion measurement method

Adhesion properties and performance are important parameters of direct printing and coating process [38-42]. There are many kinds of adhesion measurement methods. Adhesion measurement test can be divided into two broad categories – destructive or nondestructive [43]. Because of nonconstructive methods – laser or electromagnetic methods could not be applied to microstructure due to minimum size of microstructure is smaller than 50 μm, constructive methods were considered to measure adhesion properties of between nanoparticles and substrate. In this section, a shear adhesion measurement method was considered.

For measuring adhesion strength as a performance of AFN printing process, shear adhesion test was suggested. Figure 3.9 shows schematic and parameter of shear adhesion test. Procedures of suggested shear adhesion test is like below:

1) Sample imaging by SEM or optical microscopy for calculation of contact area (Figure 3.10)
2) Pt coating using sputter for measuring contact by ohm-meter
3) Measuring reference point and plane with normal vector
4) Transferring micro probe to the height (h_z) from the substrate
5) Transferring micro probe along shear direction with transfer velocity (v_s) and simultaneously measuring shear force from sensor

Adhesion test setup and close-up view are shown in Figure 3.11. The 4-axis nano-manipulator and modular control system (nano manipulater, SmartAct GmbH, Germany) were used for manipulation of substrate with test samples. For measuring shear force, dynamometer (9256C, Kistler Inc., USA) was used with micro probe (40 μm diameter tungsten carbide probe, K1 Innotek Inc., Republic of Korea). Ohm-meter was used for measuring origin point and plane using electrical resistant contact method. Before each test, Pt ion coating on both the substrate and micro probe was conducted by using Pt sputtering. The condition of Pt ion sputtering was 4 mA during 2 minutes. Shear transfer velocity, v_s, was 100 nm/s and measuring height from the substrate, h_z, was $0.1 \times D$.

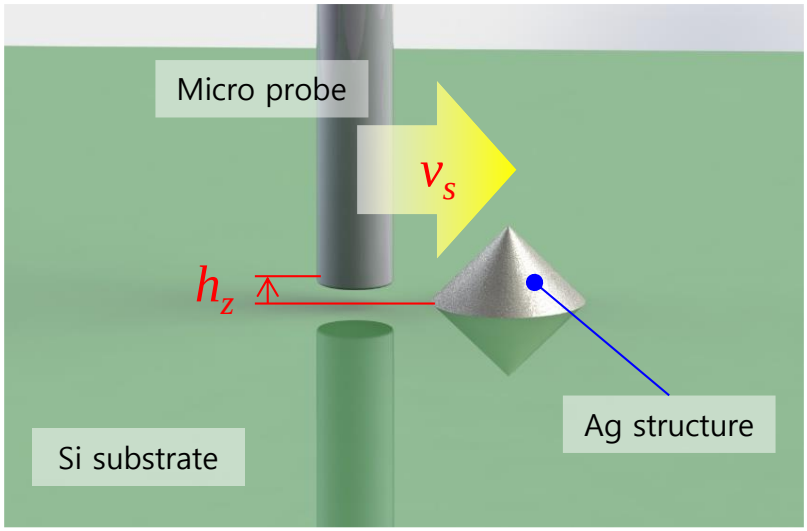

Figure 3.9. Schematic of shear adhesion test and parameters

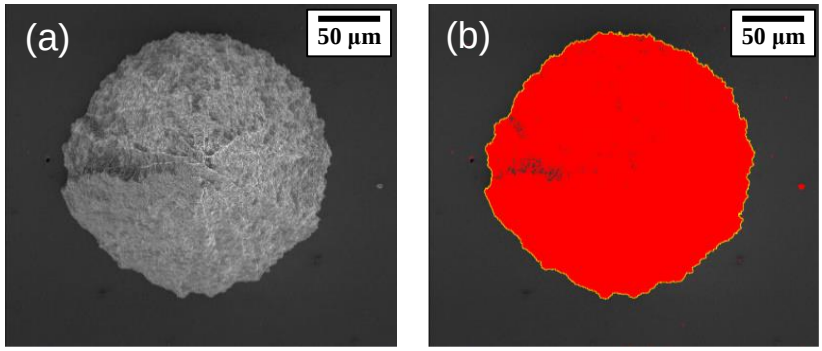

Figure 3.10. SEM images of silver microstructure; (a) a front view and (b) an image processing result from (a) using different of contrast between the substrate and silver microstructure

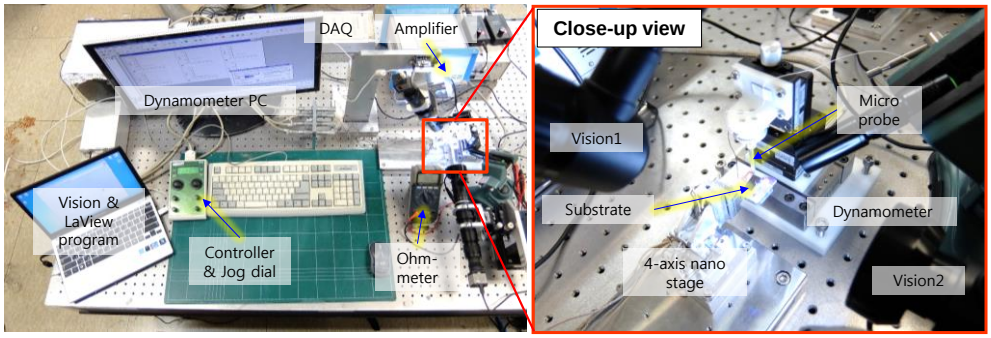

Figure 3.11. Hardware configuration of adhesion test and close-up view of test section (right)

3.3.2. Results and discussions

Figure 3.10 shows examples of result of shear force of two different size of sample from shear adhesion test during the whole test time. The magnification of two different size of samples was same. Due to different size of real contact area between microstructure and substrate, force of each sample was different.

Adhesion strength was calculated by shear force divided by contact area. The shear adhesion strength is expressed by equation (1):

$$\tau = \frac{F_{shear}}{A_{contact}} \quad \text{.....(1)}$$

Where τ is shear adhesion strength, F_{shear} is shear adhesion force when the sample is detached, and $A_{contact}$ is contact area. Figure 3.10 shows shear adhesion strength along contact area. Shear adhesion strength, τ, on the silicon wafer substrate was average 4.03 MPa. This result can be used for performance evaluation of AFN printing process and consideration in the micromachining process. However shear adhesion strength was different. If diameter or contact area were small, shear adhesion strength would be bigger than smaller samples. I seems that nanoparticle is deposited on the substrate with aerodynamically focusing effect in the early stage [10, 25]. In the result, shear adhesion strength of samples goes exponentially big as contact area goes small. Because small nanoparticles in the early stage with small focal area impact on the substrate with high speed, mechanical bonding and interfacial contact area of near center region is much high. And then nanoparticles are deposited to both microstructure generated in the early stage and substrate. In case of 20 μm diameter sample, the shear adhesion strength was 8.5 MPa, but in samples of bigger than 100 μm, the shear adhesion strength was 3.2 MPa. This result could be expressed by shear adhesion strength contour (Figure 3.12). This quantitative measurement result could be requisitely used and considered in hybrid process. Details of consideration in hybrid process is described in chapter 4.

After adhesion test, surface morphology on the substrate was investigated by SEM image (Figure 3.13). Contact boundary of detached sample is shown in Figure 3.11. (a). Remaining particles in the near center which is focal area and in the outside

from center are shown in Figure 3.13. (b) and Figure 3.13. (c), respectively. In the results, a number of remaining nanoparticles in the near center is observed (Figure 3.13. (b)) but the number of remaining nanoparticles in the outside from center was relatively small. Those are also an evidence of focal area of AFN printing and high adhesion in the center area. The local damaged shapes are also shown in Figure 3.13. (d). Local damage may be induced by impact of nanoparticle in the high velocity and aerosol shock. Because of ductile nanoparticle and brittle substrate impaction in this case, the substrate is locally damaged and destroyed. The result and morphology could be expected for using impact analysis and establishing deposition mechanism [39]. Because the substrate material has brittle and hard material properties – silicon wafer and nanoparticle has ductile and relatively mild mechanical properties, it seems that collision and erosion occurred in the early stage of the deposition, and then nanoparticle is deposited and agglomerated each nanoparticles.

For observing interfacial morphology, FIB was used for cutting the sample. Figure 3.14 shows an example of sample before cutting and after cutting in Figure 3.14. (a) and Figure 3.14. (b), respectively. Figure 3.15 shows tilt image of cut sample by FIB with high magnification image of near center area (Figure 3.15. (a)) and high magnification image far from center (Figure 3.15. (b)). In case of near center (Figure 3.15. (a)), interfacial layer between nanoparticles and substrate seems that it has hard mechanical locking comparison of anther image which is far from center (Figure 3.15. (b)). It is expected to contribute high adhesion strength in the focal area. Also it could be used for mechanical nanoscale welding [44]. These results could be helpful to not only hybrid process but also AFN printing and other direct dry nanoparticle deposition processes in terms of deposition mechanism and principle.

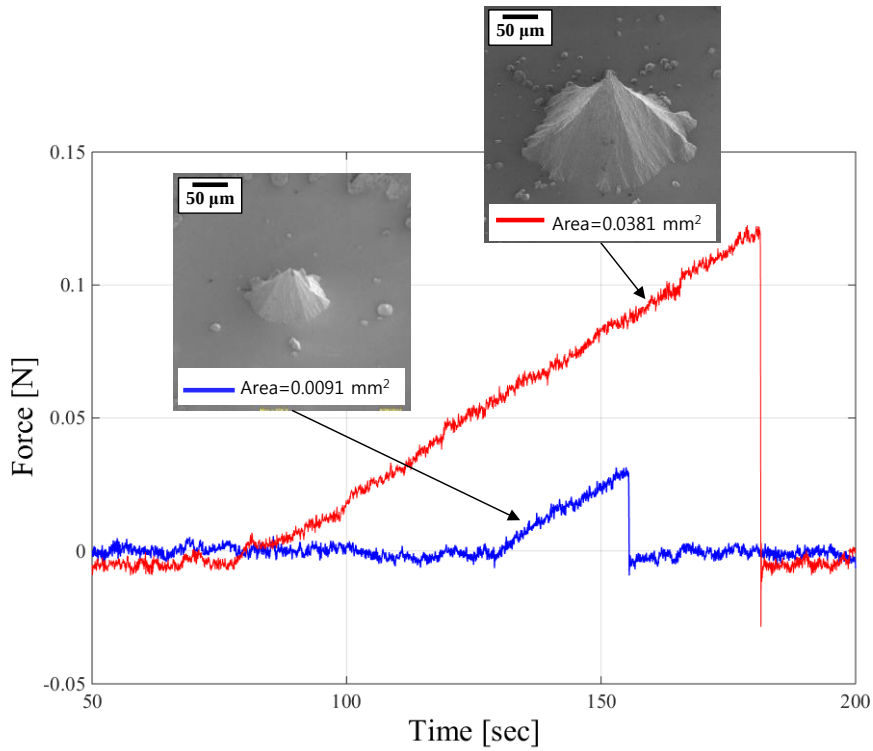

Figure 3.12. Shear force versus time result of two different size of samples

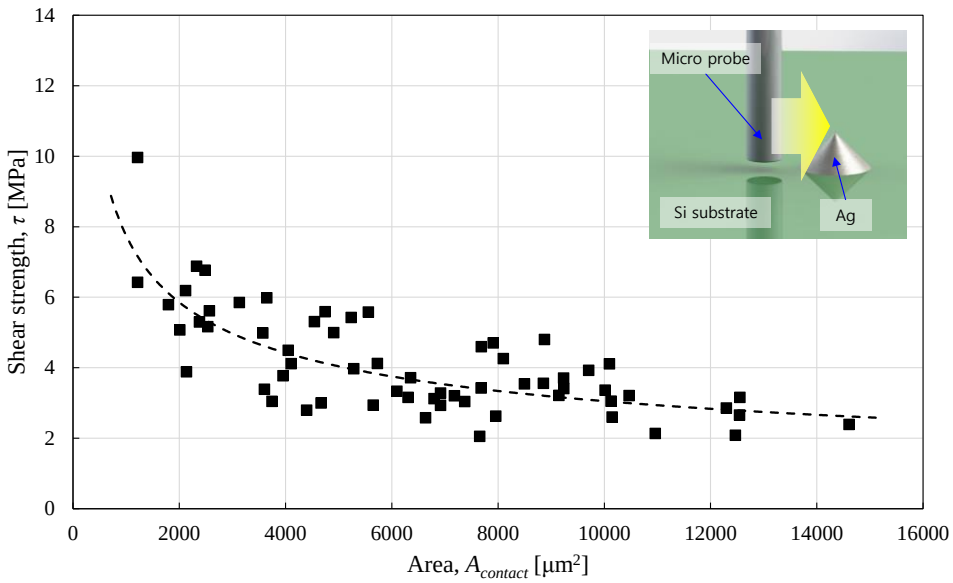

Figure 3.13. Schematic of shear adhesion test and parameters

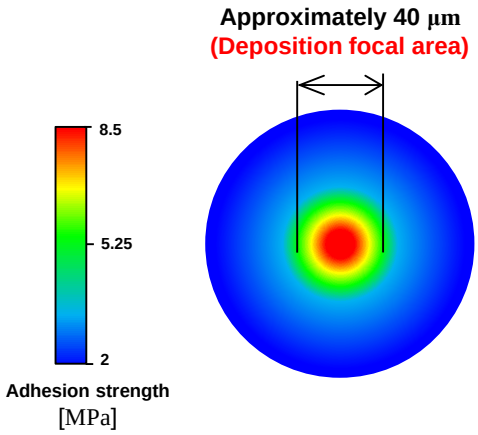

Figure 3.14. Shear adhesion strength contour of silver nanoparticle on the silicon wafer substrate

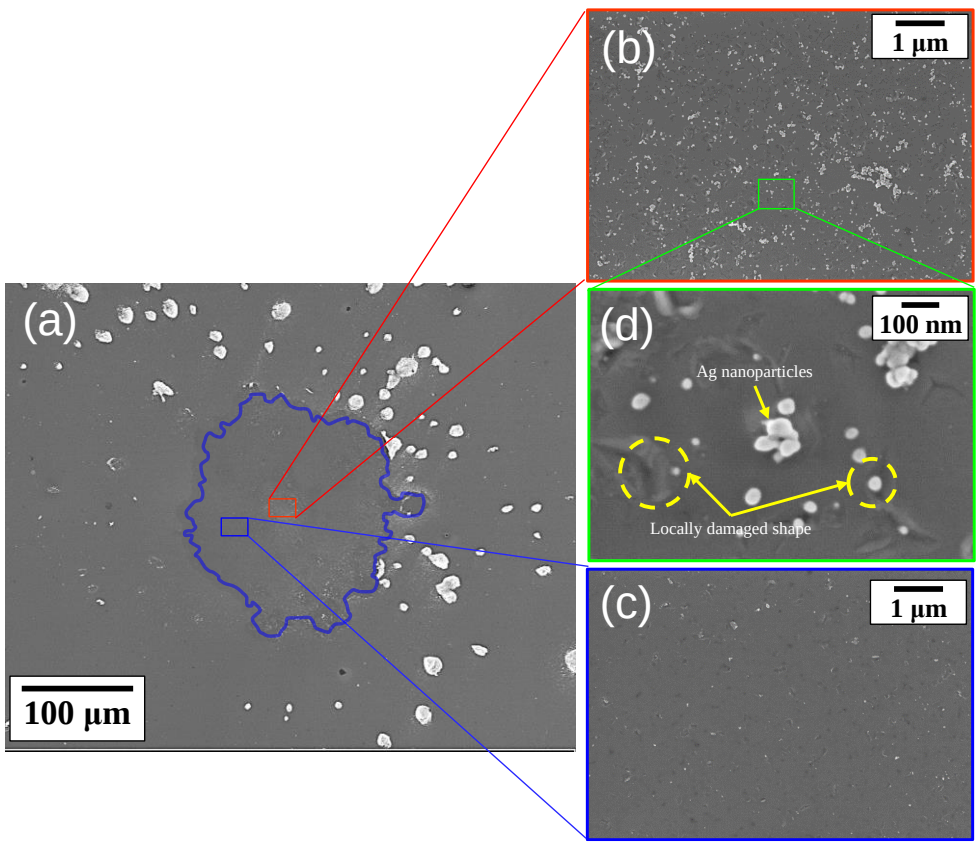

Figure 3.15. Silicon substrate after shear adhesion test; (a) contact boundary, (b) center area of contact region, (c) outside from center area region (d) high magnification image of center region with nanoparticle and locally damaged shape

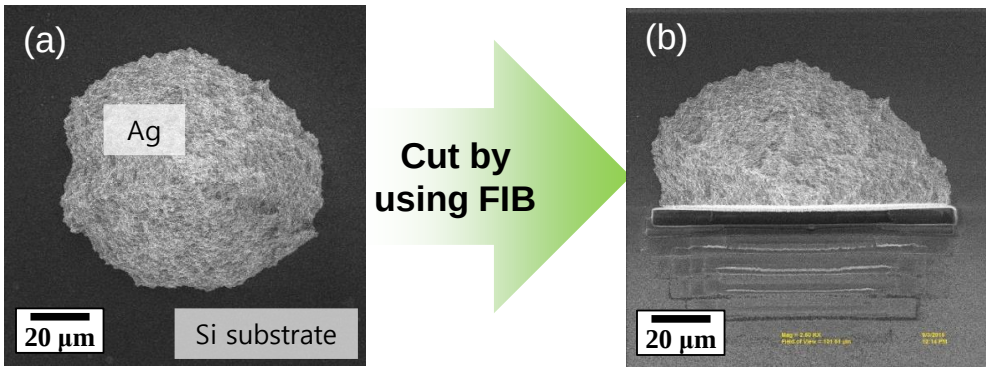

Figure 3.16. An example of silver microstructure for observing interfacial layer; (a) before cutting and (b) after cutting using FIB

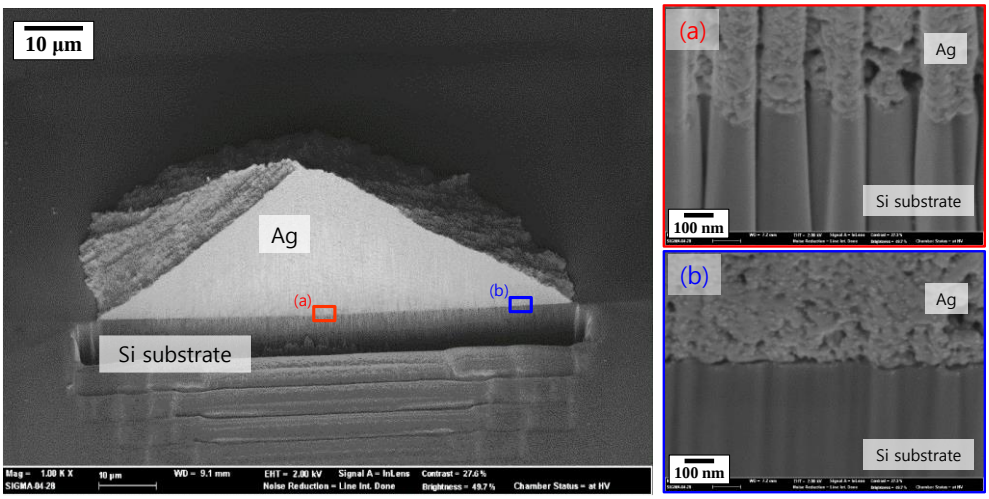

Figure 3.17. Tilt view and interfacial layer of cut sample; (a) near center area and (b) far from center area

Chapter 4. Mechanical micromachining

4.1. Process capability

The motivation for the fabrication of smaller and smaller workpieces has been essentially the same since manufacturing was first established. Machining processes have always played an important role in manufacturing or workpieces and have seen their capability for procession machining steadily improve [45]. Micro end milling is a highly flexible manufacturing process. It is for example used to machine small features in molds used for mass production, to structure medical implants for better biocompatibility, to generate deep X-ray lithography masks, and to manufacturer microfluidic devices [46, 47].

The local planarization was proposed and evaluated to silver microstructure [48]. However machining strategies was not fully defined and implemented. The existing machining method was a simple one-way moving tool path regardless of any consideration of target sample. The local planarization process did not consider cutting parameters including material removal rate (MRR) and cutting force by cutting conditions. It has occurred that machining failure was happened by fracture of microstructure or broken of target material. Hence in mechanical micromachining, machining knowledge and machining strategies are required in terms of hybrid process.

The hardware configurations of mechanical micromachining is shown in figure 4.1. Because of the accuracy of the ball bearing 3-axis stage which was initially installed in hybrid process system relatively poor than nanoscale stage, the 4-axis nano-manipulator and modular control system (nano manipulater, SmartAct GmbH, Germany) were used for the stage and the customized LabView program was used for generation of tool path. The hardware configurations were used in the all of experiments in this chapter.

As a test of mechanical micromachining process capability, an example tool path was used. The letter pattern “IDIM” tool path was generated and cut by commercial available micro milling tool (5 μm diameter with one helical edge milling tool, Performance Micro Tool, Inc., USA). PMMA (poly-methyl methacrylate) was used for the workpiece. Cutting condition of the test was like below:

- Axial depth of cut: 2 μm
- Radial depth of cut: 5 μm (diameter of tool)
- Rotational speed: 50,000 rpm
- Feed rate: 5 μm/s

The cutting condition was suggested by manufacturer. Figure 4.2 shows result of the test. Burr formation was shown in Figure 4.2. (a). Although the diameter of micro tool was 5 μm, the width of single path was 8.5 μm. Run-out of the spindle was approximately ranged 2.5 μm to 5 μm. Although the stage has high accuracy in sub-micron, it is hard to apply to ultra-precision or nano-machining due to run-out of the spindle [45]. But the axial run-out is under 1 μm, it could be used for hybrid machining including planarization process and other 2.5D structuring in microscale.

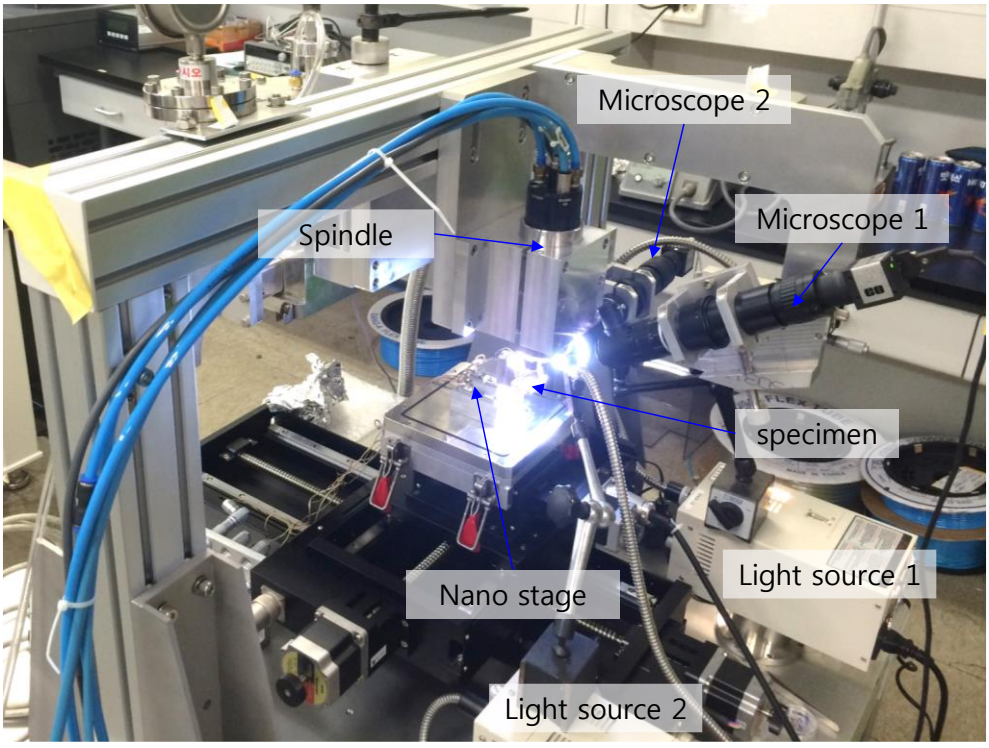

Figure 4.1. Hardware configurations of mechanical micromachining

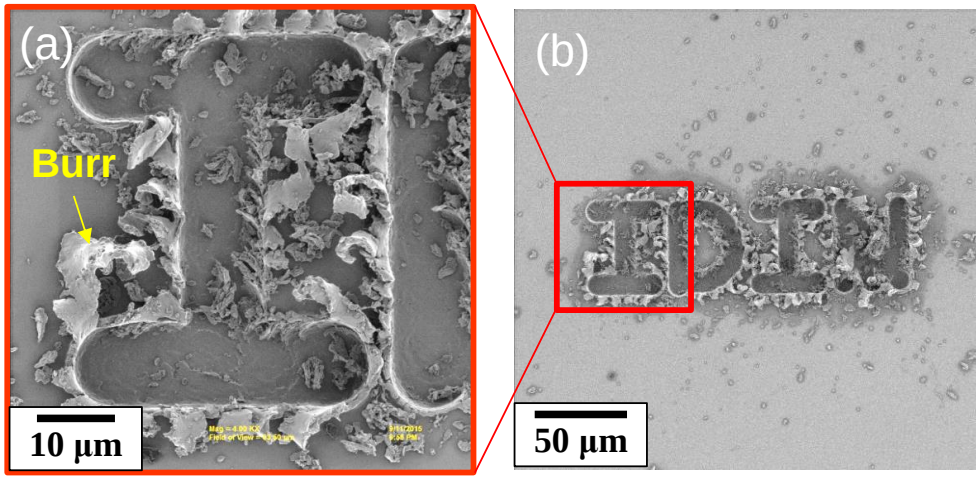

Figure 4.2. The “IDIM” letter pattern for the test of mechanical micromachining; (a) high magnification image and (b) the whole letter

4.2. Fabrication of micro tool

Micro milling tool for hybrid process can be fabricated by precision grinding, FIB, electric discharge machining (EDM), and wire-EDM [49-52]. Various planarization tools including multi-edge and single edge tool were fabricated using FIB [48]. The rotational ablation tool was fabricated by using laser machining [53]. Using multiple edge could be helpful to improve of surface quality.

In this chapter, tungsten carbide flat and plane micro-tool with 30 μm diameter with 100 μm tool length (WC plane tool, K1 Innotek Inc., Republic of Korea) was used for micromachining. The micro-tool contained 10% carbide which was ISO K10~20 grade. The mechanical properties and information of the WC micro-tool is shown in Table 4.1. The micro-tool was fabricated by FIB with multiple helical edge on which edge angle was 45°. The number of edge of tool was 10. Table 4.2 shows cutting parameters of FIB for micro milling tool. Figure 4.3 shows the micro tool fabricated by FIB.

Table 4.1. Mechanical properties and information of tungsten carbide tool

Description	Value	Unit
Grade	K200	-
ISO range	K20 ~ K50	-
WC + other carbides ratio	90	%
Cobalt ratio	10	%
WC grain size	Submicron	-
Density	14.45	g/cm^3
Hardness	92	Hra
TRS (Transverse rupture strength)	4.25	GPa
Young's modulus	550	GPa

Table 4.2. Cutting parameter of FIB for micro milling tool

Description	Value	Unit
Ion source	Gallium	-
Acceleration voltage	30	kV
Probe current	200	pA
Dwell time/pixel	20	μsec
Overlap rate	0.5	-
The number of scan	2000	-

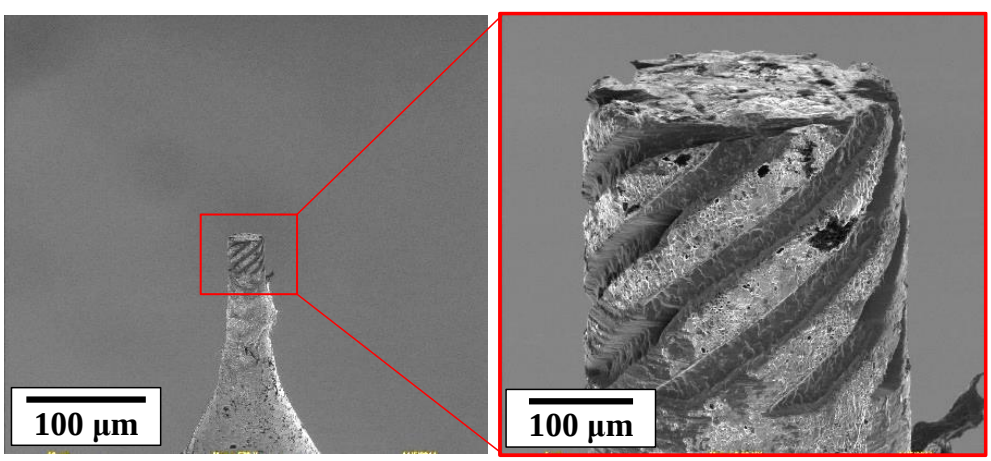

Figure 4.3. 45° helical edge micro milling tool fabricated by FIB

4.3. Machining strategies

4.3.1. Machining plane definition and modification

Because of tilt angle error of the coordinate, there are difference between stage coordinate and machining coordinate although the value is small [20]. Dimensional accuracy and surface quality are two critical aspects of manufacturing such devices. Dimensional accuracy is governed by almost the same parameters as in conventional machining. However, due to the feature size used, referencing the tool tip position to the workpiece is a bic challenge to deliver the required dimensional accuracy [54]. Therefore calibration process was proposed by the 4-point contact method. Using the 4-point contact method, machining plane can be defined. Normal and tangential vector was defined. The coordinate of the 4-point in stage coordinate reference point in center of sample (0, 0, 0) was A, B, C, and D, (-100, 100, z_A), (100, 100, z_B), (100, -100, z_C), and (-100, -100, z_D) respectively (Figure 4.4). From the z values of four points, tilt angle of the x and y axis could be defined. The reference mark or conductive line could be used for reference of tilt angle of the z axis. Figure 4.5 shows stage coordinates and calibrated machining coordinate with schematic of micromachining process.

In three axes coordinate system, calibration of tool path should be considered all of micromachining process. Because the depth direction is most important issue in the micromachining process, calibration procedure for merging two processes was required. Coordinate system transformation matrix was defined by Equation (2).

$$R_m = C_i^m R_i \quad \text{.....(2)}$$

Where $\boldsymbol{R}$ is coordinates in three axes coordinate system and $\boldsymbol{C}$ is transfer matrix. The subscript or superscript i and m mean initial and modified coordinates, respectively. In considering two dimensional case, Figure 4.6 shows that in case of the z axis rotating in ψ where initial coordinate of the x and y axis. For example, In Figure 4.6, the value of coordinate R can be expressed by $\boldsymbol{R}^i=[x_i, y_i, 0]^T$ and $\boldsymbol{R}^m=[x_m, y_m, 0]^T$. In the three dimensional case, Figure 4.7 shows unit vectors of rectangular coordinates including initial (stage) unit vectors and modified (machining) unit vectors. Unit vector of the x, y and z is expressed as $\boldsymbol{i}$, $\boldsymbol{j}$, and $\boldsymbol{k}$ respectively. The modified

coordinate, $\boldsymbol{R}_m$ in case of Figure 4.8 can be expressed by Equation (3).

$$\begin{aligned} x_m &= x_i \cos\psi + y_i \sin\psi \\ y_m &= y_i \cos\psi - x_i \sin\psi \end{aligned} \quad \cdots\cdots (3)$$

The two dimensional coordinate transfer matrix in case of Figure 4.6 is expressed by Equation (4).

$$C_i^m = C_z(\psi) = \begin{bmatrix} \cos\psi & \sin\psi \\ -\sin\psi & \cos\psi \end{bmatrix} \quad \cdots\cdots (4)$$

Tilt angles of each the x, y and z axis were θ, ϕ, and ψ, respectively. Using the coordinate system transformation matrix, micromachining can be calibrated by dot product at the initial tool path coordinate. In the three dimensional coordinate system transformation matrix can be expressed by Equation (5).

$$C_i^m = \begin{bmatrix} \cos\theta\cos\psi & \cos\phi\sin\theta\cos\psi - \cos\phi\sin\psi & \cos\phi\sin\theta\sin\psi + \sin\phi\sin\psi \\ \cos\theta\sin\psi & \sin\phi\sin\theta\sin\psi + \cos\phi\cos\psi & \cos\phi\sin\theta\sin\psi - \sin\phi\cos\psi \\ -\sin\theta & \sin\phi\cos\theta & \cos\phi\cos\theta \end{bmatrix} \quad \cdots\cdots (5)$$

Figure 4.8 shows stage plane (red, solid) and measured machining plane (blue, dash) for micromachining in three dimensional view. In the result, maximum tilt angle was 42.97 arcsec. Although the error value is quite small, it have to be considered in hybrid process for better accuracy and quality. Also the result can be used for the coordinate system transformation of tool path. These machining plane definition and modification strategies were used in this chapter.

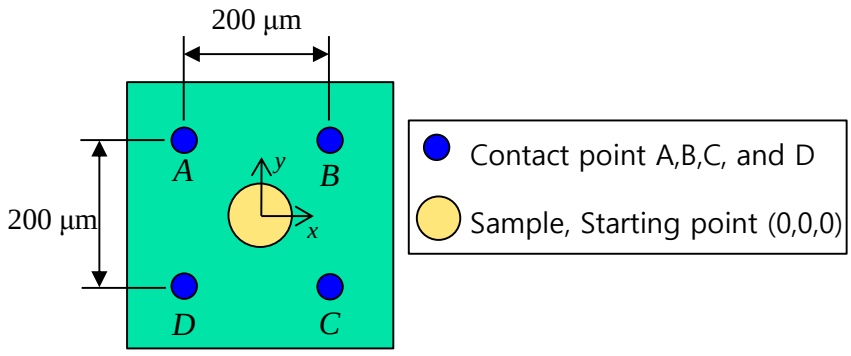

Figure 4.4. Schematic of the 4-point contact to define machining plane

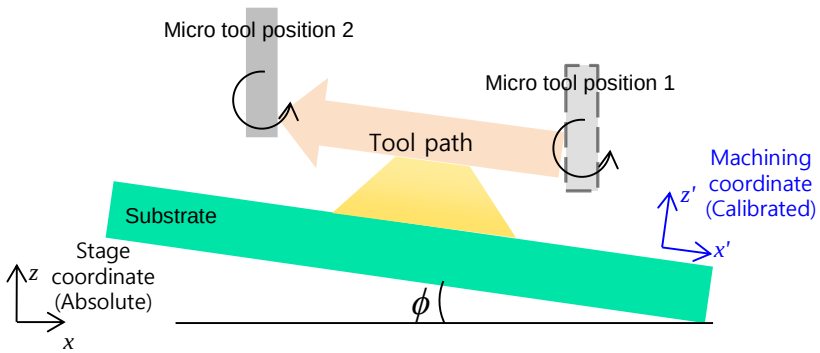

Figure 4.5. Schematic of calibrated machining tool path

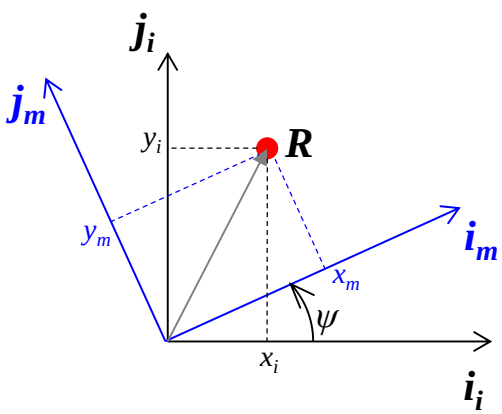

Figure 4.6. An example of rotating the z axis as ψ in the x-y plane

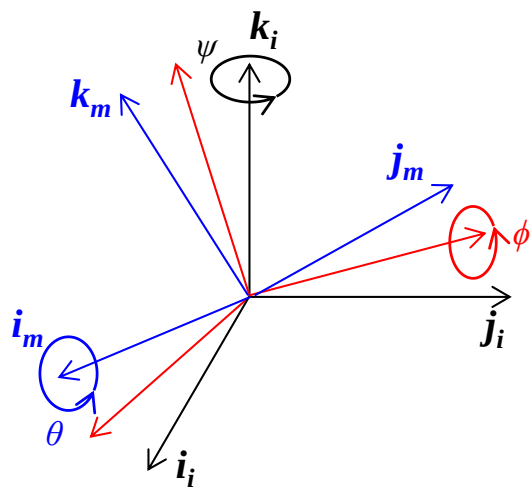

Figure 4.7. Unit vectors of rectangular coordinates

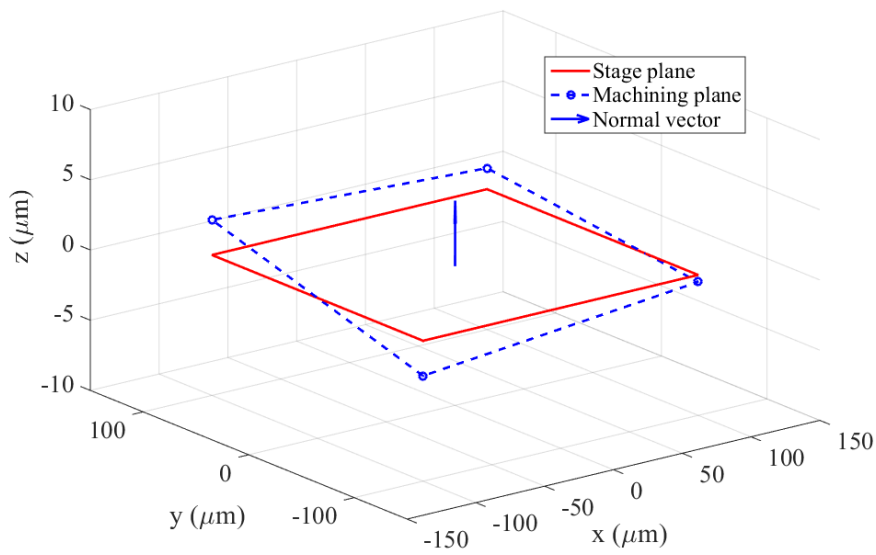

Figure 4.8. Machining plane with normal vector

4.3.2. Slot milling

For planarization of the top on the micro width conductive line fabricated by AFN printing, slot milling was used. This process was used for fabrication of micro-electronics supported by FIB [8, 12]. Figure 4.8 shows slot milling tool path and calibrated tool path strategy. The tool path was generated from geometrical model in chapter 4. The cutting condition of slot milling was like below:

- Axial depth of cut: 1 μm
- Radial depth of cut: 30 μm (diameter of tool)
- Rotational speed: 60,000 rpm
- Feed rate: 2 μm/s

The cutting was conducted by using integrated hybrid machine. Target height from the substrate was ranged from 10 μm to 20 μm. The existing planarization strategy could not fabricated under 20 μm repeatedly. Figure 4.9 shows an example of the result after slot milling on the conductive silver line. Burr formation and surface quality could be verified in Figure 4.9. (a) and Figure 4.8. (b), respectively. The surface after machining was observed as high quality with dense surface comparted with before machining. Surface roughness, Ra, of the machining surface was under 50 nm. Furthermore, Figure 4.10 shows the micro tool condition after slot milling tests. The number of machining samples was 10. The debris and tool wear were observed in Figure 4.10. Tool wear and cutting condition have to be investigated in the near future for more improvement of process.

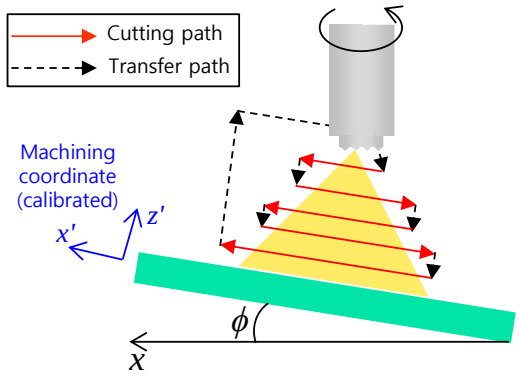

Figure 4.9. Schematic of slot milling path and calibrated strategy

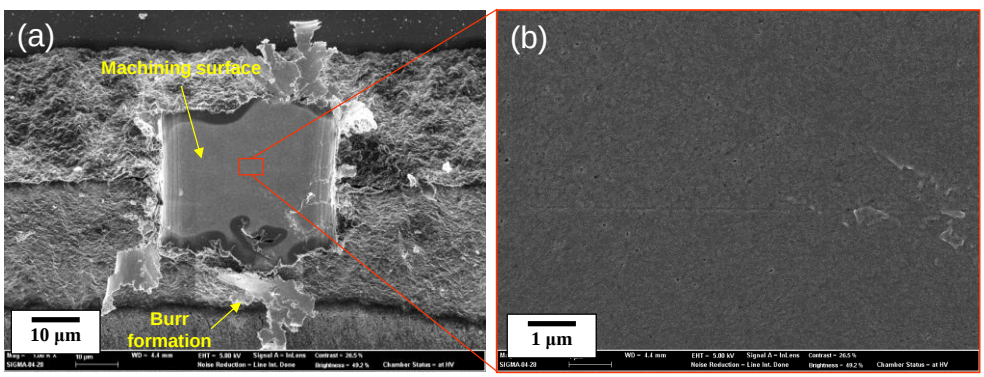

Figure 4.10. The result after slot milling on silver conductive line; (a) front view and burr formation and (b) high magnification of ground surface

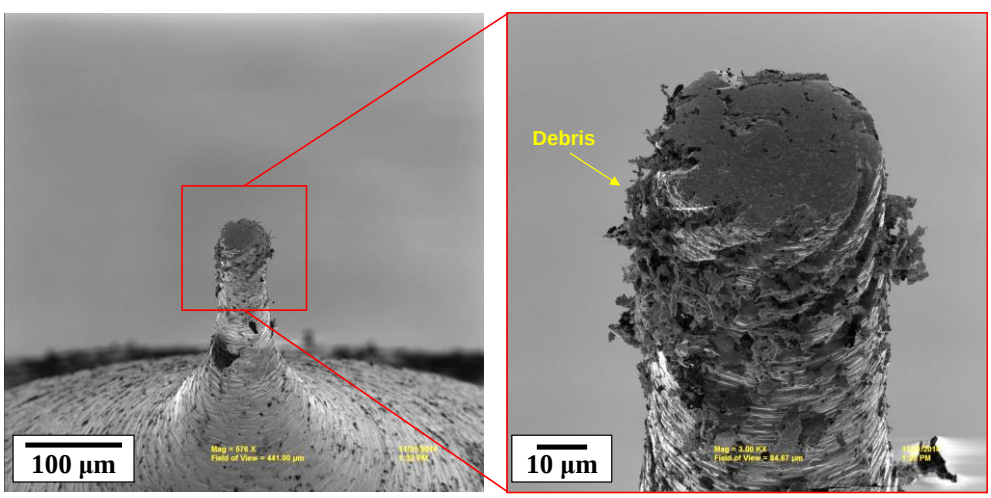

Figure 4.11. Tilt view of micro tool after slot milling process

4.3.2. Face milling

For ground surface of microstructure after deposition by AFN printing to flat and high surface accuracy, face milling was used. Face milling process was used for fabrication of nanoscale multi-material structure [8] and for measuring mechanical properties of hybrid process [55]. Figure 4.11 shows cutting strategies of face milling process as a schematic. In order to improve accuracy and roughness, zigzag tool path was used for face milling (Figure 4.11). The cutting conditions were like bellow:

- Axial depth of cut: 0.5 μm
- Radial depth of cut: 2 μm
- Rotational speed: 80,000 rpm
- Feed rate: 3.33 μm/s

For the evaluation of micromachining process, SEM image and confocal microscopy were used (Figure 4.12 and Figure 4.13). Figure 4.12 shows comparison of sample both before face milling and after face milling in Figure 4.12. (a) and Figure 4.12. (b), respectively. The tool mark was observed in Figure 4.9. (c). It seems that uncertain vibration or high feed rate might occur. Figure 4.13 shows a result of confocal microscopic image. Surface roughness, Ra, was under 50 nm and height repeatability was under 1 μm. Few of burr formation was observed in this case and surface quality was better than slot milling in this case because MRR is lower than slot milling although same material was used in each case. Consequently, small MRR affect miniaturizing burr formation. It might improve process quality. Figure 4.14 shows an example of debris after face milling. Debris was agglomerated and detached from the sample.

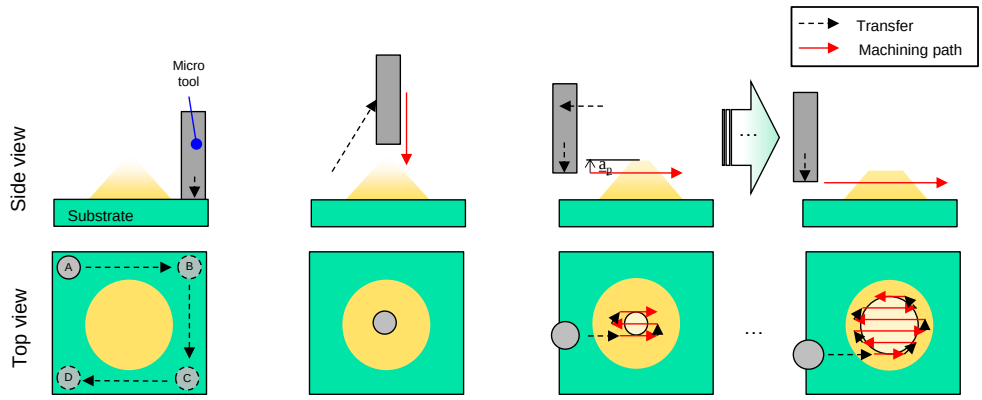

Figure 4.12. Schematic of face milling procedure and tool path

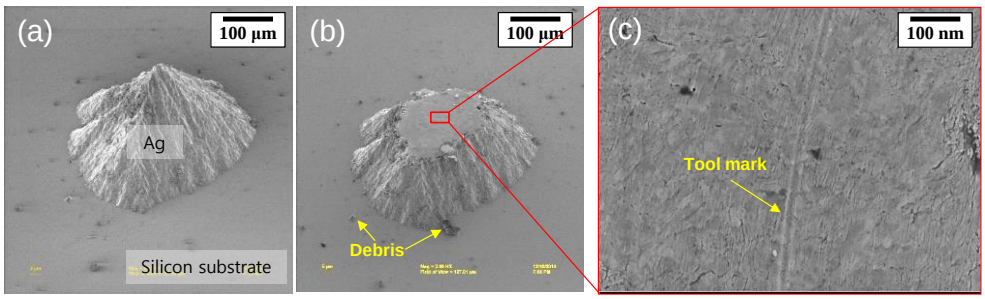

Figure 4.13. Surface morphology after hybrid process; (a) before face milling, (b) after face milling, and (c) high magnification surface after machining with tool mark

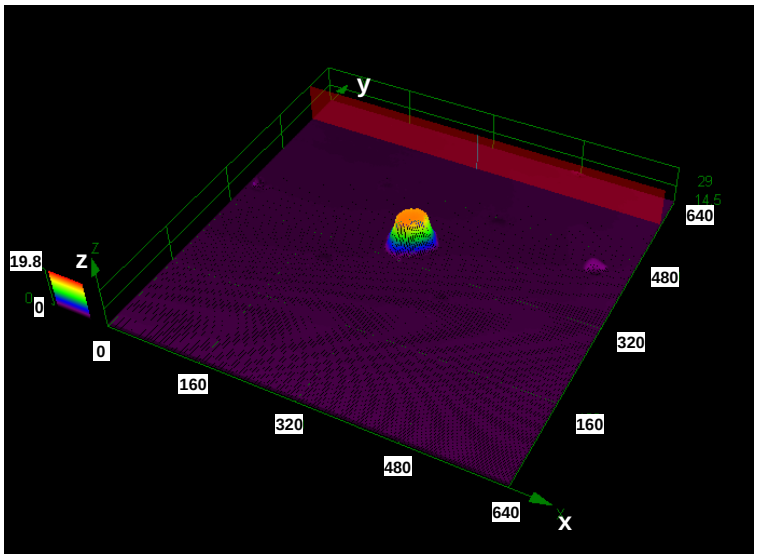

Figure 4.14. The result of confocal microscopic image after face milling

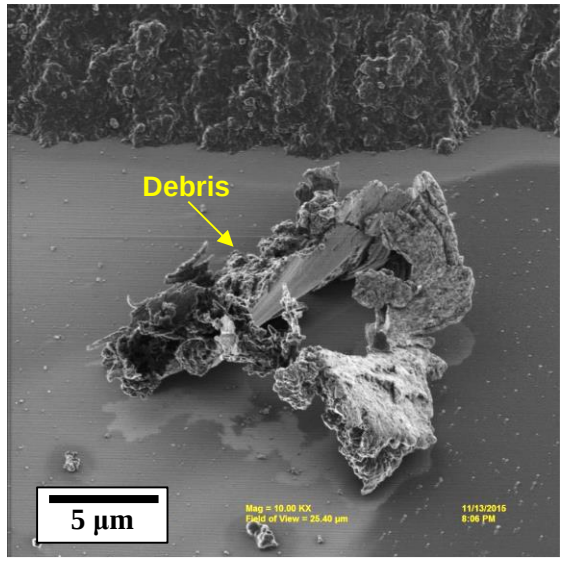

Figure 4.15. Silver debris after face milling

4.4. Mechanical properties

4.4.1. Nano indentation

Nano indentation test was used for evaluation mechanical properties of the hybrid process material. XP Berkovich tip (diamond, 20 nm radius) was used for nano indentation. Three different samples which have different height were tested in order to whether different mechanical properties show or not along height from the substrate. Heights of three samples were 30 μm, 25 μm, and 20 μm, at sample A, sample B, and sample C, respectively. Initial height of initial samples before face milling process was 46 μm. Samples were fabricated by hybrid process which was AFN printing and face milling sequence. Indentation depth was 2 μm in the all of sample. Nano indentation parameters are shown in Table 4.3. Because indentation depth is bigger than sample thickness, data may be influenced by substrate. Nano indentation test were three times in each sample.

4.4.2. Results and discussions

Figure 4.15 shows result of an example of the top of measured surface after nano indentation test. The test result of nano indentation is shown in Figure 4.16. The result shows properties of each sample is different by height. The height means sample height from substrate of the sample after machining. Figure 4.17 shows results of hardness and modulus according to height. The average value of hardness and modulus of bulk silver is 0.65 GPa and 86 GPa, respectively [56]. The results shows hardness and modulus of silver after hybrid process account for averagely approximately 75% and 17% respectively compared with bulk silver material. Especially modulus is remarkably low. It may be characteristics of porous structure of dry nanoparticle deposition process.

Mechanical properties of material and workpiece are important in micromachining and hybrid process because it affects cutting conditions and quality [20, 57]. As a similar test with nano indentation, compression test of micro pillar of silver structure fabricated by NPDS and planarization process was investigated [55]. In the study, micro pillar was cut by using FIB. The yield strength, modulus and ultimate stress were 28.5 MPa, 0.42 GPa, and 87.19 MPa, respectively. Table 4.4 shows comparison of mechanical properties of silver including hybrid process.

Table 4.3. Nano indentation test parameters

Description	Value	Unit
Surface approach velocity	10	nm/s
Depth limits	200	nm
Strain rate	0.05	s-1
Harmonic displacement	2	nm
Frequency	45	Hz
Surface approach distance	1000	nm

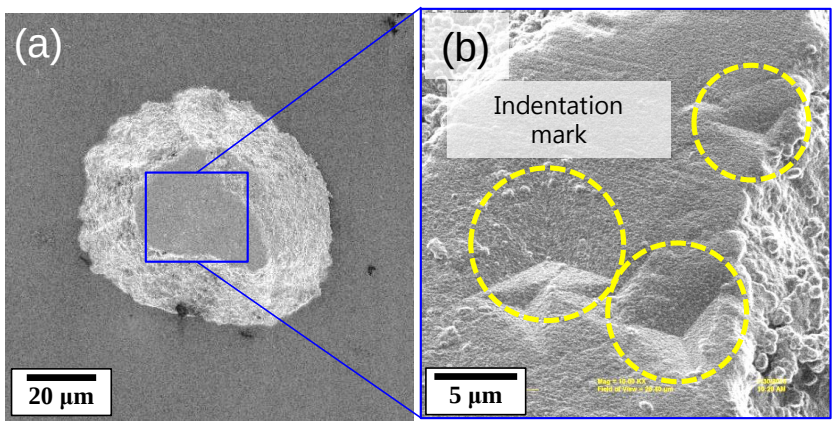

Figure 4.16. Microstructure after nano indentation; (a) front view and (b) high magnification image with indentation mark

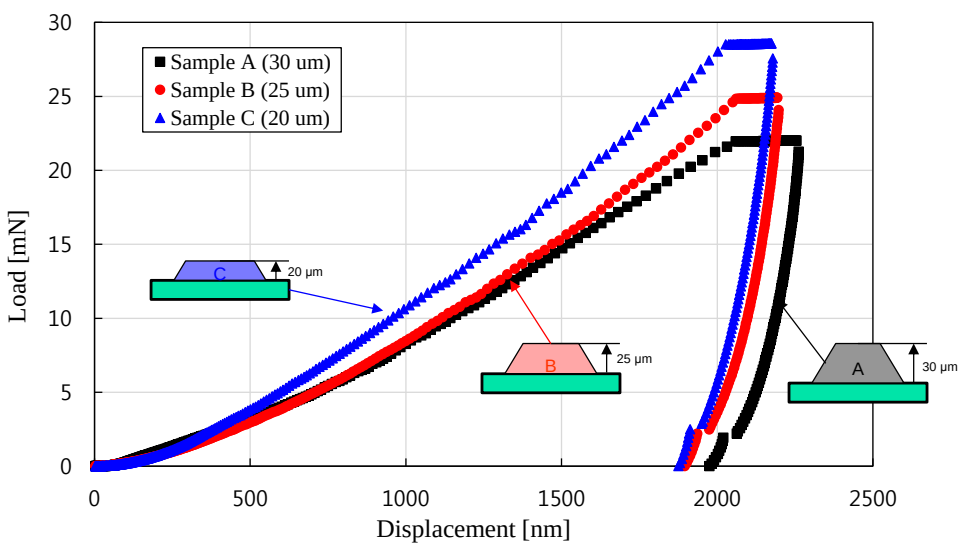

Figure 4.17. Load versus displacement in different samples

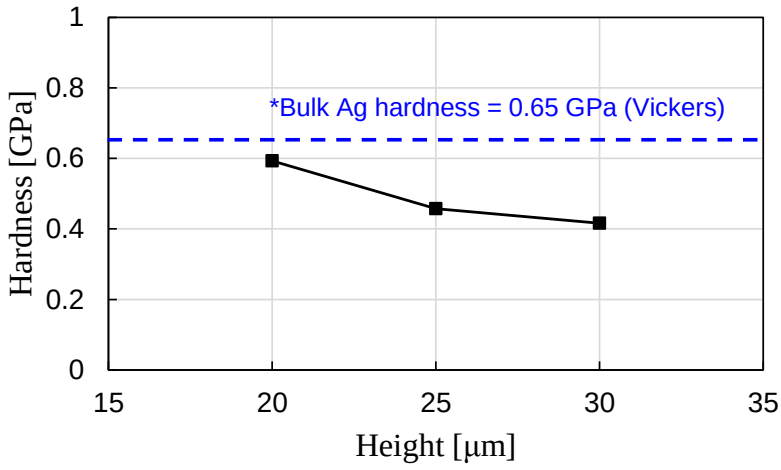

(a)

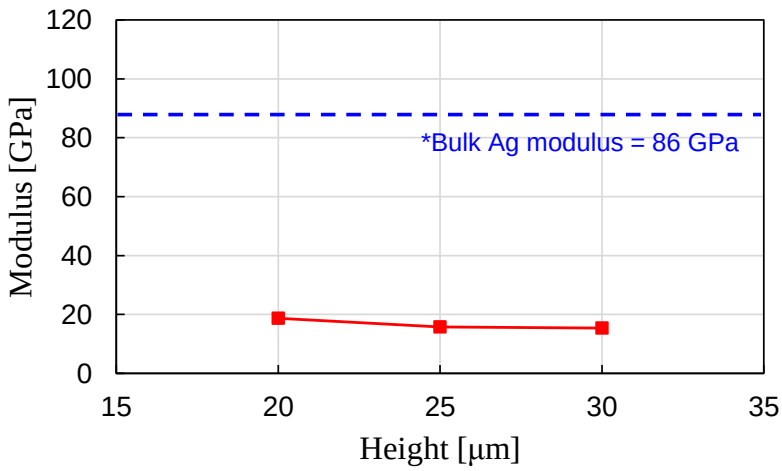

(b)

Figure 4.18. Nano indentation test results according to height; (a) hardness and (b) modulus

Table 4.4. Comparison of mechanical properties of silver (Ag)

Properties	Bulk [56]	Hybrid process	
		Micro compression [55]	Nano indentation
Hardness [GPa]	0.65	-	0.485
Modulus [GPa]	100	0.42	16.59

Chapter 5. Hydrophobic characteristics

5.1. Overview

Wetting occurs when a solid–gas interface transitions to a solid–liquid interface on a solid surface. Control of material wettability is a key issue in surface engineering [58]. Superhydrophobic surfaces with a high static contact angle greater than 150°, and contact angle hysteresis (the difference between the advancing and receding contact angles) less than 10°, exhibit extreme water repellence and self-cleaning properties [59]. Interest in superhydrophobic surface increased after the discovery of the self-cleaning properties of lotus leaves, depending on their hierarchical roughness. It has been found that superhydrophobicity can be engineered in micro- and nanostructures with a low surface energy [60].

Dry nanoparticle deposition processes, particularly aerodynamically focused nanoparticle (AFN) printing, can be used to fabricate hierarchical structures. As AFN printing deposits nanoparticles by high speed impact, various inorganic materials can be printed on a substrate without the use of bonding chemicals or heat treatment. However, printed features show an uneven surface with a nanoscale roughness, and a porous structure. The surface morphology of silver microstructures was investigated in Chapter 3. Surface roughness can be controlled by a hybrid process. As discussed in Chapter 4, planarization and polishing processes can be used to control surface roughness through additional mechanical micromachining.

In this chapter, the fabrication of hydrophobic surfaces by AFN printing is investigated and analyzed. The anisotropic surface contact angle and superhydrophobicity were varied through control of the AFN-printed lattice pattern parameters. The micro-groove pattern, and quadrangle width, were also found to affect the anisotropic contact angle. Passive control of the contact angle by a hybrid process was also investigated through micromachining the top surface of the microstructure.

5.2. Superhydrophobic and anisotropic surfaces

5.2.1. Experimental detail

A droplet deposition and imaging system was developed to measure the contact angle and hydrophobicity of the fabricated microstructure patterns. An inkjet head (MD-K 130, Microdrop Technologies GmbH, Norderstedt, Germany) was used to deposit a droplet on the surface, a 3-axis stage (SGSP20, Sigma Koki, Tokyo, Japan) was used to manipulate the sample position, and two charge couple device (CCD) cameras (EO-0813C, Edmond Optics, Barrington, NJ, USA) imaged the droplet. Figure 5.1 shows the hardware configuration for contact angle measurement. An inkjet controller was used to deposit a specific droplet volume. Table 5.1 shows the inkjet parameters for the creation of distilled water microdroplets. The two cameras were used to measure the contact angle from orthogonal positions.

To measure the precise contact angle, the low-bond axisymmetric drop shape analysis (LB-ADSA) method was used [61]. Open source ImageJ software (National Institutes of Health, Bethesda, MD, USA) and a plug-in program was used for LB-ADSA.

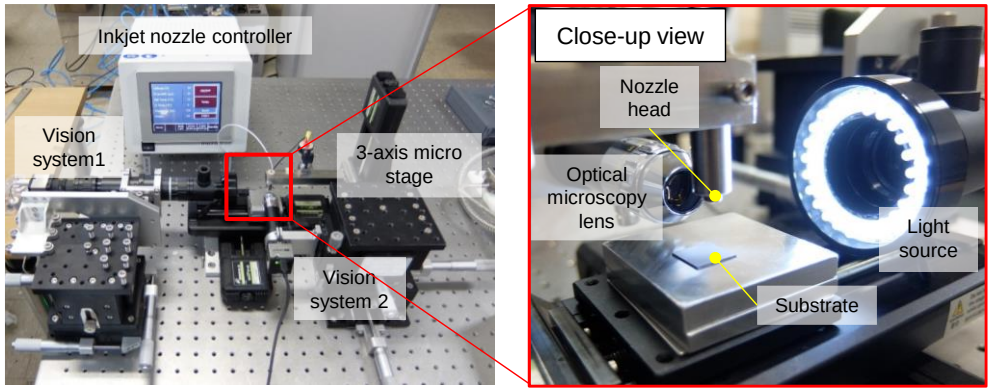

Figure 5.1. The hardware configuration for contact angle measurement

Table 5.1. The process parameters used for inkjet printing of the microdroplets

Description	Value	Unit
Fluid	Distilled water	-
Input voltage	93	V
Pulse width	33	μsec
Diameter of minimum droplet	65	μm

5.2.2. Superhydrophobic surface

Several lattice patterns were fabricated by AFN printing using silver nanoparticles on the silicon wafer substrate. Figure 5.2 shows the profile and contact angle of 0.56 µL water droplets on two substrates. Figure 5.2(a) shows the water droplet on a silicon wafer substrate, which had been cleaned using ethanol. The contact angle was 57.02º. Figure 5.2(b) shows the water droplet on a 300 µm silver lattice pattern. The contact angle was 161.5º, indicating a superhydrophobic surface. The contact angle of a water droplet on pure silver is reported to be 90º [62]. The nanoscale roughness of the silver microstructure may not only contribute to the hierarchical structure, but also to the superhydrophobic surface.

Figure 5.3 shows an example of a patterned superhydrophobic surface. The effect of the lattice pattern width on the hydrophobicity was studied. Water droplets of varying volume were measured on samples with lattice patterns from 100 µm to 500 µm in 100 µm intervals. Figure 5.4 shows the static contact angle as a function of droplet volume for each of the lattice patterns. Owing to the wide lattice pattern, a sudden decrease in contact angle was observed for the 400 µm and 500 µm samples. The contact angle increased as the droplet volume increased. The water droplet contact angle as a function of pattern interval is plotted in Figure 5.5. The contact angle decreased when the pattern interval was greater than 300 µm, whereas a superhydrophobic surface was observed for samples in which the spacing was less than 300 µm.

These results suggest that AFN printing can be used to modify hydrophobic surfaces, and it could be possibly used for the fabrication of self-cleaning surfaces, or lab-on-a-chip applications.

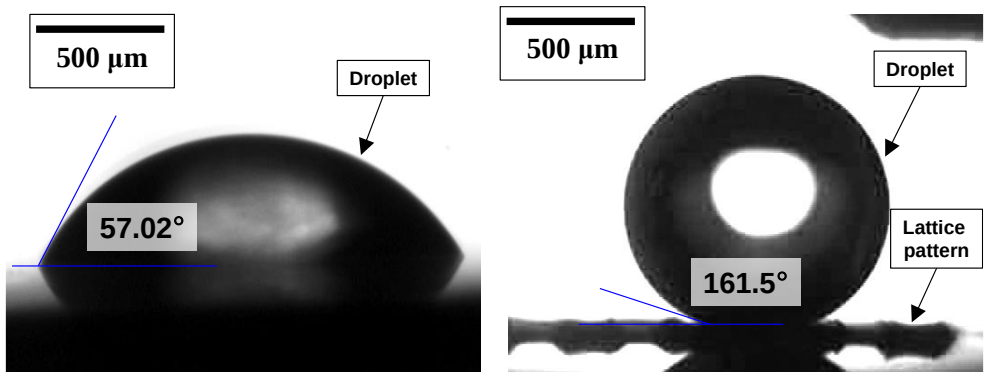

(a) (b)

Figure 5.2. Images showing the water droplet profile and contact angle when placed on (a) a silicon wafer, and (b) on a 300 µm lattice pattern

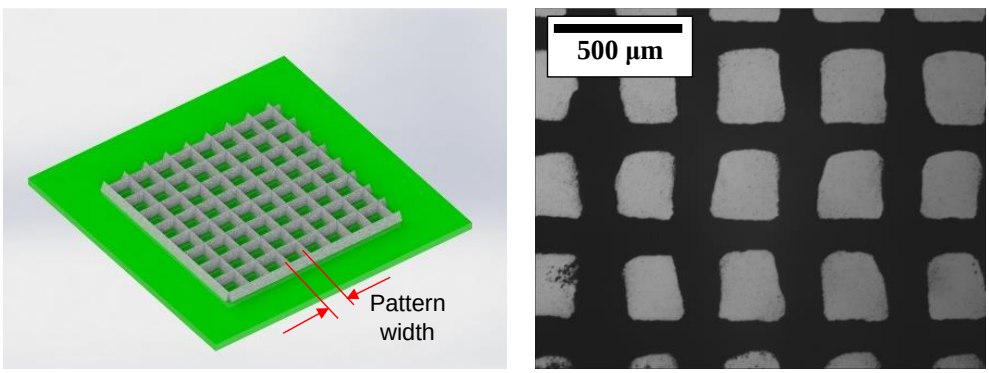

(a) (b)

Figure 5.3. An example of a superhydrophobic surface; (a) schematic of lattice pattern and (b) an image of 300 µm lattice pattern

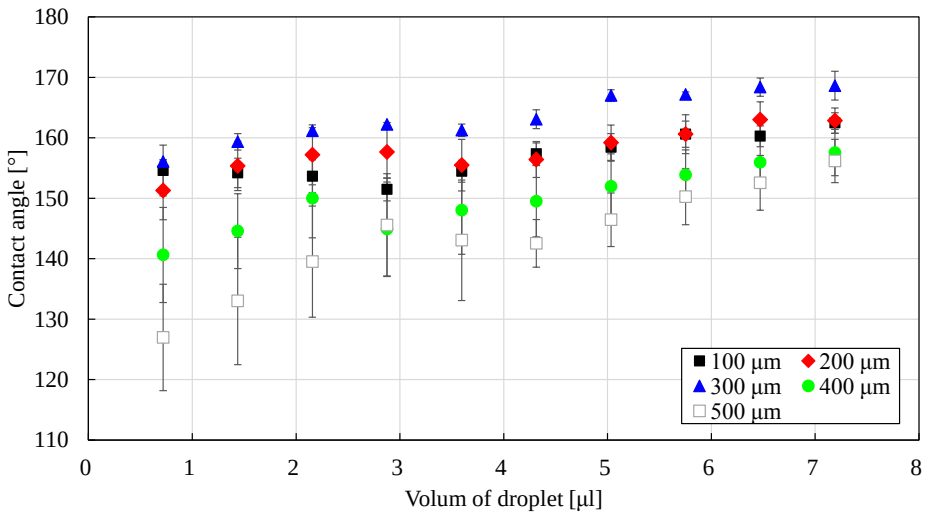

Figure 5.4. The static contact angle of water droplets on silver lattice patterns

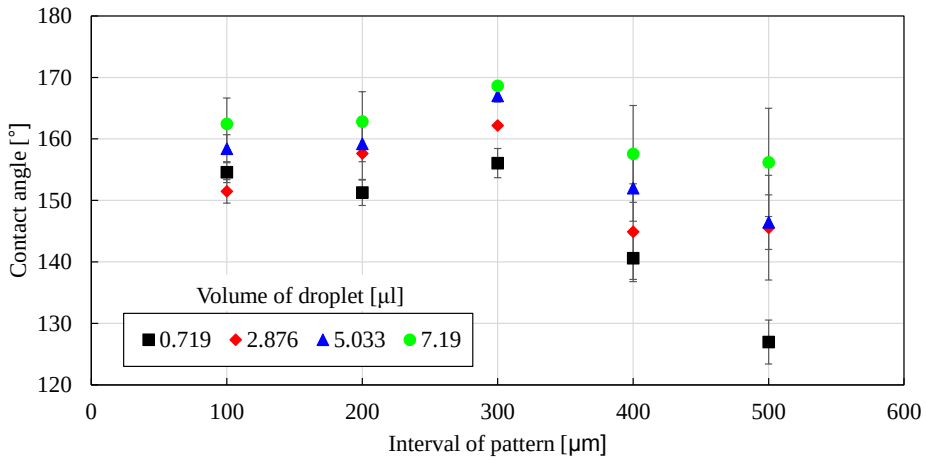

Figure 5.5. Static water droplet contact angle on silver lattice patterns, according to pattern interval

5.2.2. Anisotropic contact angle

Anisotropically textured surfaces have directional properties that provide the basis for a wide range of applications [63]. Samples were fabricated with anisotropic patterns, and their hydrophobicity was tested.

A quadrangle pattern was used to produce an anisotropic surface contact angle with width w. Figure 5.6 shows a schematic of the quadrangle pattern, and the position of the cameras. Two cameras were used to measure the anisotropic surface contact angles. In the experiment, the length *l* was fixed at 150 μm, and *w* was varied from 150 μm to 350 μm in 50 μm intervals. The experimental details were the same as those described in Section 5.1 of this chapter. Figure 5.7 shows the quadrangle structure contact angle as a function of width. The contact angle of the 150 μm × 150 μm angle of the rectangle structure did not change. As the width was increased, the contact angle was reduced. As the silver structure is hierarchical, it has hydrophobic properties, whereas the silicon wafer is hydrophilic.

Horizontal micro-grooving patterns were used to create the anisotropic hydrophobic surface. A schematic of the 100-μm-wide micro-groove patterns is given in Figure 5.8. Figure 5.9 shows the static contact angle of the micro-groove patterns, from both camera positions, as a function of water droplet size. The contact angle recorded by the camera focused on the pattern cross-section (camera 1 in Figure 5.8) was much greater, although both cameras indicated a superhydrophobic surface contact angle.

Figure 5.10 shows images of the dynamic rolling test. Figure 5.10(a) shows the sliding angle parallel to the pattern (camera 2), and Figure 5.10(b) shows the sliding angle orthogonal to the pattern (camera 1). These results show that hydrophobicity can be controlled by the pattern interval and shape. Anisotropic superhydrophobicity for the control of microscale will be studied further.

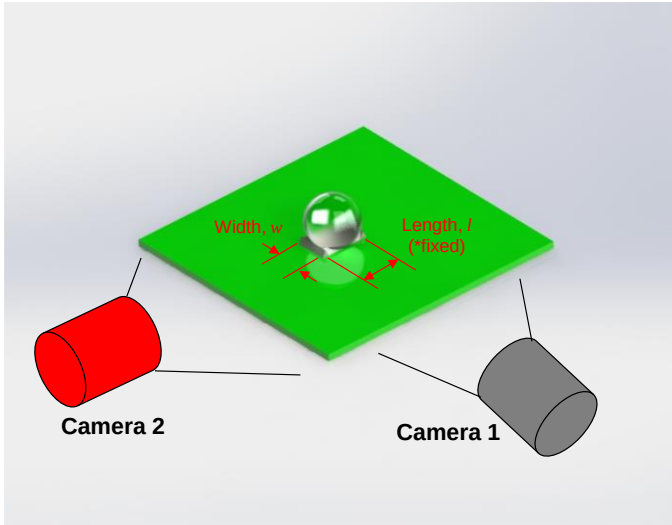

Figure 5.6. Schematic of the quadrangle pattern and vision systems, with length *l* and width *w* indicated

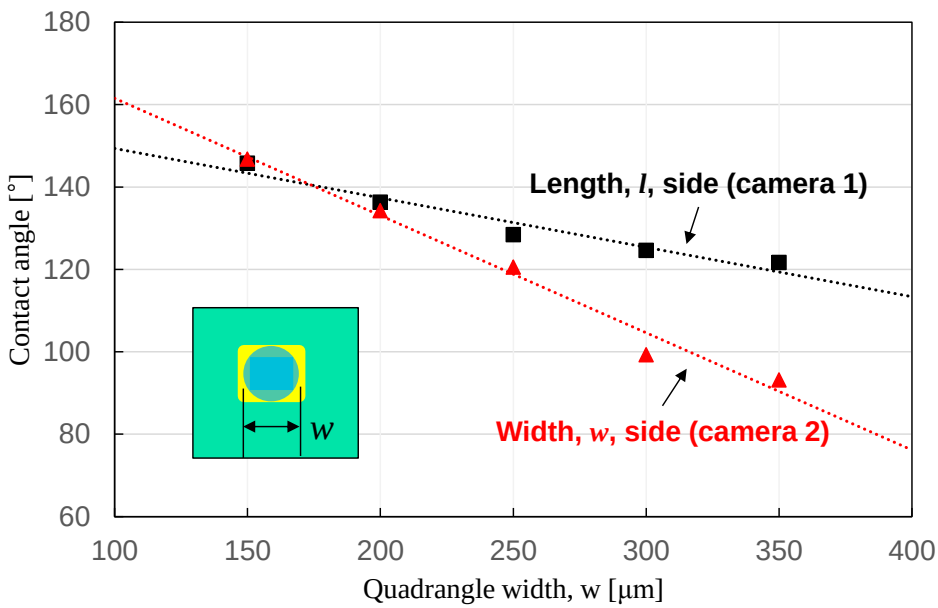

Figure 5.7. Anisotropic contact angles of the quadrangle structure

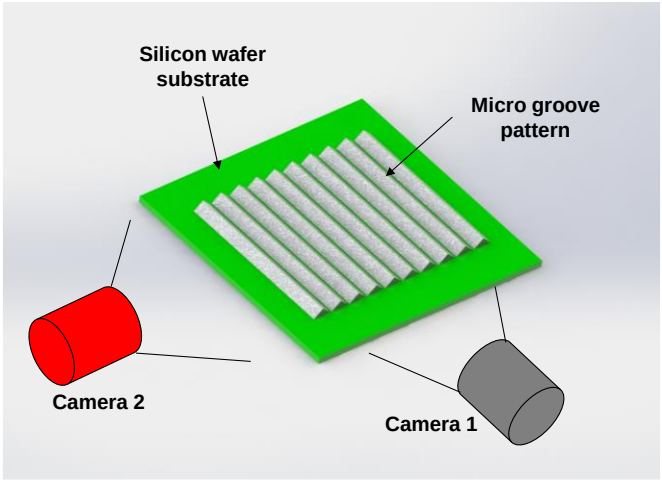

Figure 5.8. Schematic of the micro-groove pattern and cameras

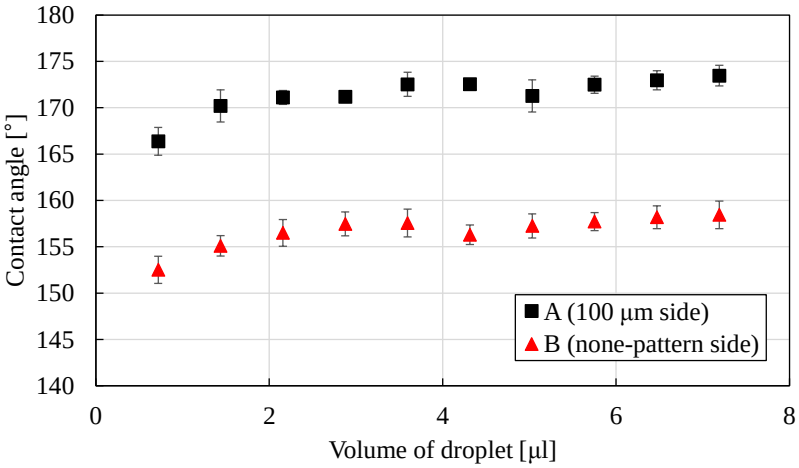

Figure 5.9. Static contact angle of the microgroove patterns

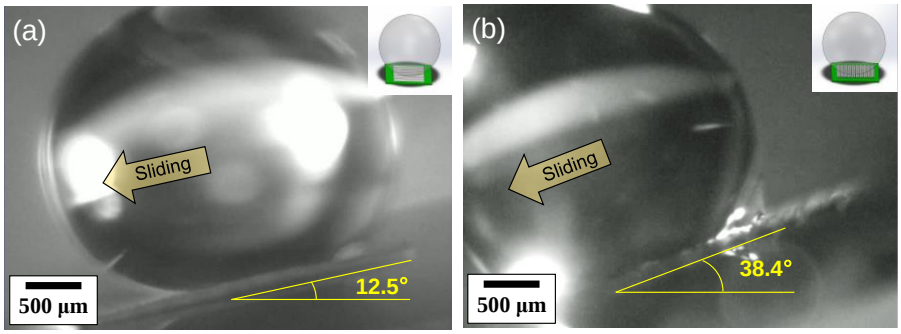

Figure 5.10. Comparison of the droplet sliding angles when viewed from two positions; (a) parallel to the groove direction, and (b) perpendicular to the groove direction

5.2. Passive control of hydrophobicity

The control of surface morphology using hybrid processes was investigated. AFN printing can be used to fabricate microscale structures with roughened and porous nanoscale surfaces. In hybrid processing, the surface quality and morphology can be changed by the effects of micromachining, as discussed in Chapters 3 and 4. It was expected that hydrophobicity could be passively controlled.

Silver microstructures were fabricated by AFN printing, and the surface was milled to modify the shape and quality. The inkjet system was used to generate and deposit microscopic water droplets. Figure 5.11(a) shows the water droplet profile and contact angle immediately after deposition. Figure 5.11(b) shows the contact angle after 4.2 s. The droplet contact angle changes as a result of evaporation. Figure 5.12 shows the variation of the contact angle over time, changing from a hydrophobic to a hydrophilic angle. The contact angle between pure silver and water in the air was 90° [62]. The results suggest that the surface was hydrophilic after micromachining. Using hybrid processing, the change in, and control of, the surface contact angle was verified.

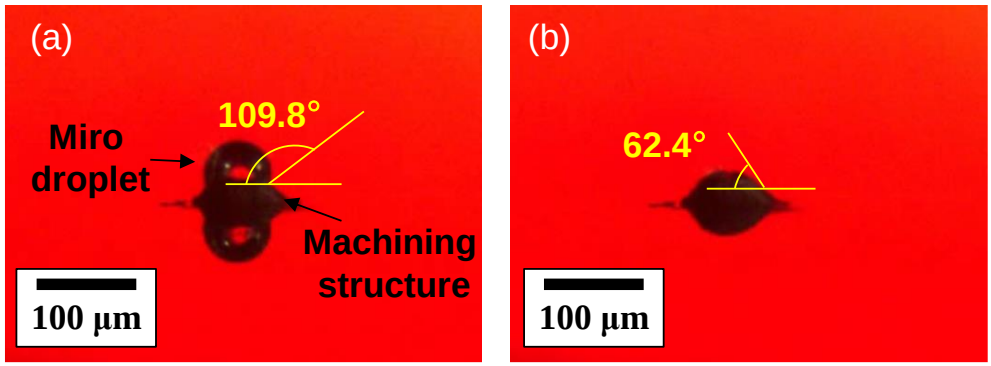

Figure 5.11. Change in contact angle on the top of microstructure; (a) initial state and (b) after 4.2 s

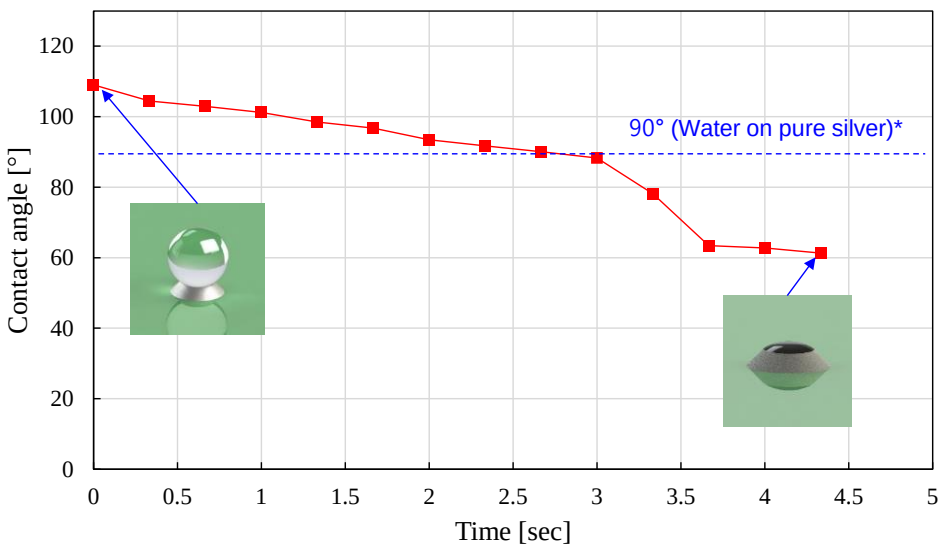

Figure 5.12. Surface contact angle plotted as a function of time

Chapter 5. Conclusions

A microscale hybrid process was integrated with additive AFN printing, and subtractive mechanical micromachining.

The deposition and adhesion characteristics of AFN printing were analyzed. The relationship between diameter and height was investigated. Erosion and collision were the primary mechanisms in the early stages of the deposition process. An adhesion test was proposed to evaluate the performance of the AFN printing process, and measurements were made. The average shear adhesion strength of a silver nanoparticle on a silicon wafer substrate was 4.03 MPa. However, the shear adhesion strength near the center of the particle was stronger than at the periphery, due to the aerodynamic focus effect. The surface morphology after removal of a sample was investigated. Hard-bonded remnants of the nanoparticle were observed. These results are expected to further understanding of deposition and adhesion mechanisms.

Micromachining strategies were suggested that included the definition of a machining plane, and a coordinate system transformation matrix was defined using the four-point contact method. Slot milling and face milling methods using a calibrated machining plane were proposed. Confocal microscopy was used to measure the micromachining performance. Height control in the hybrid process was less than 1 μm, and the surface roughness (Ra) was less than 50 nm. The mechanical properties after hybrid processing were measured by nanoindentation. The results show that the hardness and modulus were less than those of bulk silver (0.65 GPa and 85 GPa, respectively).

Superhydrophobic surfaces with various lattice patterns were successfully fabricated using an AFN printing process. Silver nanoparticles were used to fabricate lattice patterns on the silicon wafer substrate. Water droplet contact angles were measured, and both superhydrophobic and anisotropic surfaces were demonstrated. Passive control of the surface contact angle using hybrid processes was demonstrated.

Bibliography

[1] Patil M, Mehta DS, Guvva S. Future impact of nanotechnology on medicine and dentistry. Journal of Indian Society of Periodontology. 2008;12:34.

[2] Brousseau E, Dimov S, Pham D. Some recent advances in multi-material micro-and nano-manufacturing. The International Journal of Advanced Manufacturing Technology. 2010;47:161-80.

[3] Qin Y, Brockett A, Ma Y, Razali A, Zhao J, Harrison C, et al. Micro-manufacturing: research, technology outcomes and development issues. The International Journal of Advanced Manufacturing Technology. 2010;47:821-37.

[4] Chu W-S, Kim C-S, Lee H-T, Choi J-O, Park J-I, Song J-H, et al. Hybrid manufacturing in micro/nano scale: A Review. International Journal of Precision Engineering and Manufacturing-Green Technology. 2014;1:75-92.

[5] Anitha R, Arunachalam S, Radhakrishnan P. Critical parameters influencing the quality of prototypes in fused deposition modelling. Journal of Materials Processing Technology. 2001;118:385-8.

[6] Agarwala MK, Jamalabad VR, Langrana NA, Safari A, Whalen PJ, Danforth SC. Structural quality of parts processed by fused deposition. Rapid Prototyping Journal. 1996;2:4-19.

[7] Karunakaran K, Suryakumar S, Pushpa V, Akula S. Low cost integration of additive and subtractive processes for hybrid layered manufacturing. Robotics and Computer-Integrated Manufacturing. 2010;26:490-9.

[8] Yoon H-S. Hybrid 3D printing by bridging micro/nano processes: Seoul National University; 2015.

[9] Zhu Z, Dhokia V, Nassehi A, Newman ST. A review of hybrid manufacturing processes–state of the art and future perspectives. International Journal of Computer Integrated Manufacturing.

2013;26:596-615.

[10] Lee G-Y. Multi-material direct printing by pulsed-nano particle deposition system (P-NPDS): Seoul National University; 2013.

[11] Kim C-S. Nanoscale 3D printing process using nano particle deposition system and focused ion beam: Seoul National University; 2013.

[12] Ahn S-H, Yoon H-S, Jang K-H, Kim E-S, Lee H-T, Lee G-Y, et al. Nanoscale 3D printing process using aerodynamically focused nanoparticle (AFN) printing, micro-machining, and focused ion beam (FIB). CIRP Annals-Manufacturing Technology. 2015.

[13] Ahn S, Chun D, Kim C. Nanoscale hybrid manufacturing process by nano particle deposition system (NPDS) and focused ion beam (FIB). CIRP Annals-Manufacturing Technology. 2011;60:583-6.

[14] Lauwers B, Klocke F, Klink A, Tekkaya AE, Neugebauer R, McIntosh D. Hybrid processes in manufacturing. CIRP Annals - Manufacturing Technology. 2014;63:561-83.

[15] Weiss LE, Prinz FB, Siewiork DP. A framework for thermal spray shape deposition: The MD* system. Solid Freeform Fabrication Symposium Proceedings1991. p. 178-86.

[16] Kietzman J. Rapid prototyping polymer parts via shape deposition manufacturing: Stanford University; 1999.

[17] Lanzetta M, Cutkosky MR. Shape deposition manufacturing of biologically inspired hierarchical microstructures. CIRP Annals - Manufacturing Technology. 2008;57:231-4.

[18] Fessler J, Nickel A, Link G, Prinz F, Fussell P. Functional gradient metallic prototypes through shape deposition manufacturing. Proceedings of the solid freeform fabrication symposium1997. p. 521-8.

[19] Kim J, Cho K, Hwang J, Iurascu C, Park F. Eclipse-RP: a new RP machine based on repeated deposition and machining. Proceedings of the Institution of Mechanical Engineers, Part K: Journal of Multi-body Dynamics. 2002;216:13-20.

[20] Hur J, Lee K, Kim J. Hybrid rapid prototyping system using machining and deposition. Computer-Aided Design. 2002;34:741-54.

[21] Chu WS, Kim SG, Jung WK, Kim HJ, Ahn SH. Fabrication of micro parts using nano composite deposition system. Rapid Prototyping Journal. 2007;13:276-83.

[22] Fujita J, Ishida M, Ichihashi T, Ochiai Y, Kaito T, Matsui S. Growth of three-dimensional nano-structures using FIB-CVD and its mechanical properties. Nuclear Instruments and Methods in Physics Research Section B: Beam Interactions with Materials and Atoms. 2003;206:472-7.

[23] Zakharov D, Lebedev G, Irzhak A, Afonina V, Mashirov A, Kalashnikov V, et al. Submicron-sized actuators based on enhanced shape memory composite material fabricated by FIB-CVD. Smart Materials and Structures. 2012;21:052001.

[24] Igaki J-y, Kanda K, Haruyama Y, Ishida M, Ochiai Y, Fujita J-i, et al. Comparison of FIB-CVD and EB-CVD growth characteristics. Microelectronic Engineering. 2006;83:1225-8.

[25] Lee GY, Park JI, Kim CS, Yoon HS, Yang J, Ahn SH. Aerodynamically focused nanoparticle (AFN) printing: novel direct printing technique of solvent-free and inorganic nanoparticles. ACS applied materials & interfaces. 2014;6:16466-71.

[26] Chun D-M, Ahn S-H. Deposition mechanism of dry sprayed ceramic particles at room temperature using a nano-particle deposition system. Acta Materialia. 2011;59:2693-703.

[27] Bala N, Singh H, Karthikeyan J, Prakash S. Cold spray coating process for corrosion protection: a review. Surface Engineering. 2014;30:414-21.

[28] Hon K, Li L, Hutchings I. Direct writing technology—Advances and developments. CIRP Annals-Manufacturing Technology. 2008;57:601-20.

[29] Hoey JM, Lutfurakhmanov A, Schulz DL, Akhatov IS. A review on

aerosol-based direct-write and its applications for microelectronics. Journal of Nanotechnology. 2012;2012.

[30] Ghelichi R, Guagliano M. Coating by the cold spray process: a state of the art. Fracture and Structural Integrity. 2009:30-44.

[31] Champagne VK, Helfritch DJ. Mainstreaming cold spray – push for applications. Surface Engineering. 2014;30:396-403.

[32] Kim Y, Yang S, Lee J-W, Choi J-O, Ahn S-H, Lee CS. Photovoltaic Characteristics of a Dye-Sensitized Solar Cell (DSSC) Fabricated by a Nano-Particle Deposition System (NPDS). Materials Transactions. 2013;54:2064-8.

[33] Chun D-M. Development of nano particle depoisition system (NPDS) for room temperature deposition of metals and ceramics and its applications: Seoul National University; 2010.

[34] Chun D-M, Choi J-O, Lee CS, Kanno I, Kotera H, Ahn S-H. Nano-particle deposition system (NPDS): Low energy solvent-free dry spray process for direct patterning of metals and ceramics at room temperature. International Journal of Precision Engineering and Manufacturing. 2012;13:1107-12.

[35] Uddin MA, Alam MO, Chan YC, Chan HP. Adhesion strength and contact resistance of flip chip on flex packages—effect of curing degree of anisotropic conductive film. Microelectronics Reliability. 2004;44:505-14.

[36] Klinkov SB, Kosarev VF, Rein M. Cold spray deposition: Significance of particle impact phenomena. Aerospace Science and Technology. 2005;9:582-91.

[37] Chu HJ. Simulation of particle deposition in NPDS using SPH theory: Seoul National University; 2014.

[38] Bhushan B. Adhesion and stiction: Mechanisms, measurement techniques, and methods for reduction. Journal of Vacuum Science & Technology B: Microelectronics and Nanometer Structures.

2003;21:2262.

[39] Assadi H, Gärtner F, Stoltenhoff T, Kreye H. Bonding mechanism in cold gas spraying. Acta Materialia. 2003;51:4379-94.

[40] Maboudian R. Critical Review: Adhesion in surface micromechanical structures. Journal of Vacuum Science & Technology B: Microelectronics and Nanometer Structures. 1997;15:1.

[41] Goldbaum D, Shockley JM, Chromik RR, Rezaeian A, Yue S, Legoux J-G, et al. The Effect of Deposition Conditions on Adhesion Strength of Ti and Ti6Al4V Cold Spray Splats. Journal of Thermal Spray Technology. 2011;21:288-303.

[42] KAŠPAROVÁ M, VOLÁK J, ZAHÁLKA F, HOUDKOVÁ Š. Shear Strength of Thermally Sprayed Coatings. Mater Sci Eng. 1998;251:166.

[43] Lacombe R. Adhesion measurement methods: theory and practice: CRC Press; 2005.

[44] Choi J-O, Kim C-S. Nanoscale patterning and welding by solvent-free dry particle spray and focused ion beam. International Journal of Precision Engineering and Manufacturing-Green Technology. 2014;1:257-60.

[45] Dornfeld D, Min S, Takeuchi Y. Recent Advances in Mechanical Micromachining. CIRP Annals - Manufacturing Technology. 2006;55:745-68.

[46] Zhi Z-l, Morita Y, Hasan Q, Tamiya E. Micromachining microcarrier-based biomolecular encoding for miniaturized and multiplexed immunoassay. Analytical chemistry. 2003;75:4125-31.

[47] Filiz S, Xie L, Weiss LE, Ozdoganlar OB. Micromilling of microbarbs for medical implants. International Journal of Machine Tools and Manufacture. 2008;48:459-72.

[48] Bilegt E. Evaluation of planarization process of nanostructure deposited by nano particle deposition system (NPDS): Seoul National University; 2014.

[49] Cheng X, Wang Z, Kobayashi S, Nakamoto K, Yamazaki K. Development of a computer assistant programming system for micro/nano milling tool fabrication by multi-axis wire EDM. International Journal of Computer Integrated Manufacturing. 2009;22:847-56.

[50] Aurich JC, Reichenbach IG, Schüler GM. Manufacture and application of ultra-small micro end mills. CIRP Annals - Manufacturing Technology. 2012;61:83-6.

[51] Adams DP, Vasile MJ, Benavides G, Campbell AN. Micromilling of metal alloys with focused ion beam–fabricated tools. Precision Engineering. 2001;25:107-13.

[52] Cheng X, Wang Z, Nakamoto K, Yamazaki K. A study on the micro tooling for micro/nano milling. The International Journal of Advanced Manufacturing Technology. 2011;53:523-33.

[53] Kim M-H, Kim H-J, Kim NN, Yoon H-S, Ahn S-H. A rotational ablation tool for calcified atherosclerotic plaque removal. Biomedical microdevices. 2011;13:963-71.

[54] Min S, Sangermann H, Mertens C, Dornfeld D. A study on initial contact detection for precision micro-mold and surface generation of vertical side walls in micromachining. CIRP Annals - Manufacturing Technology. 2008;57:109-12.

[55] Lee H-T, Kim C-S, Yoon H-S, Jang K-H, Choi J-O, Ahn S-H. In-situ Characterization of Nano-structures fabricated by focused ion beam (FIB) and nano particle deposition system (NPDS). the ASME 2014 International Design Engineering Technical Conferences & Computers and Information in Engineering Conference. Buffalo, New York, US: ASME; 2014.

[56] Howatson AM. Engineering tables and data: Springer Science & Business Media; 2012.

[57] Inamura T, Takezawa N, Kumaki Y. Mechanics and Energy Dissipation

in Nanoscale Cutting. CIRP Annals - Manufacturing Technology. 1993;42:79-82.

[58] Quéré D. Wetting and roughness. Annu Rev Mater Res. 2008;38:71-99.

[59] Bhushan B, Jung YC, Koch K. Micro-, nano- and hierarchical structures for superhydrophobicity, self-cleaning and low adhesion. Philosophical transactions Series A, Mathematical, physical, and engineering sciences. 2009;367:1631-72.

[60] Celia E, Darmanin T, Taffin de Givenchy E, Amigoni S, Guittard F. Recent advances in designing superhydrophobic surfaces. Journal of colloid and interface science. 2013;402:1-18.

[61] Stalder AF, Melchior T, Muller M, Sage D, Blu T, Unser M. Low-bond axisymmetric drop shape analysis for surface tension and contact angle measurements of sessile drops. Colloids and Surfaces A: Physcochem Eng Aspects. 2010;364:72-81.

[62] Young HD, Freedman RA, Ford L. Sears and Zemansky's university physics: Pearson education; 2006.

[63] Malvadkar NA, Hancock MJ, Sekeroglu K, Dressick WJ, Demirel MC. An engineered anisotropic nanofilm with unidirectional wetting properties. Nature materials. 2010;9:1023-8.

초 록

기술이 진보함에 따라서 상용제품의 다기능성, 고집적화 그리고 신뢰성을 구현하기 위한 제조와 공정기술이 발전하고 있다. 특히 이를 위하여 마이크로와 나노스케일 제조공정과 기술은 다양한 분야에서 널리 사용된다. 그러나 단일 제조공정은 크기와 재료의 제한, 제작 가능한 형상과 품질의 한계가 있다. 이런 단점들을 보완하기 위하여 두 가지 혹은 그 이상의 공정을 융합하여 구현할 수 있는 하이브리드 제조공정이 널리 사용되고 활발히 연구되고 있다.

본 논문에서는 두 가지 서로 다른 적층공정 (additive process)과 절삭공정 (subtractive process)를 융합하여 마이크로스케일 하이브리드 공정을 구현하였다. 적층공정으로 건식 나노적층 공정의 한 종류인 공기역학적 나노입자 집속 인쇄 (aerodynamically focused nanoparticle printing) 장치가 사용되었다. 절삭공정으로는 기계식 마이크로 머시닝 공정이 사용되었다. 서로 다른 두 공정을 하나의 플랫폼으로 구성하였으며 각 공정의 특성과 하이브리드 가공에서 나타나는 현상을 탐구하였다.

나노입자의 적층과 응착 특성에 대한 연구를 수행하였다. 적층 특성으로는 적층 모양과 패턴의 특징을 연구하였으며, 적층 성능을 평가하기 위하여 응착성 시험을 수행하였다. 전단응착강도를 정량적으로 측정하였으며 평가 후 전자주사현미경을 이용한 나노입자의 적층 형상이 관찰되었다.

하이브리드 공정에서 마이크로머시닝을 구현하기 위한 네 점 접촉을 통한 가공면 설정법이 정의되었다. 다중 나선 날 (multi-helical edges) 텅스텐 카바이드 마이크로 툴이 집속 이온빔 (focused ion beam)을 이용하여 제작되었다. 마이크로 구조물의 정면 평탄화와 은 (silver) 도선의 슬롯 밀링을 위한 마이크로머시닝 가공전략이 각각 제안되었으며 가공성이 평가되었다. 하이브리드 공정을 거친 후 마이크로 구조물의 기계적 물성치가 나노 압입시험 (nanoindentation)을 통하여 평가되었다.

공기역학적 나노입자 집속 인쇄장치를 이용하여 제작된 다양한 격자 패턴으로 초소수성 표면 (superhydrophobic surface)이 구현되었다. 마이크로 그루브 (microgroove) 패턴을 이용하여 이방성 (Anisotropic)을 갖는 소수성 표면을 확인하였다. 하이브리드 공정을 통하여 수동적으로 표면 접촉각이 제어될 수 있음을 확인하였다. 본 연구를 통한 결과물은 하이브리드 제조기술과 다양한 응용에 활용될 수 있는 가능성을 보였다.

주요어: 하이브리드 가공, 공기역학적 나노입자 집속 인쇄, 마이크로 머시닝, 소수성 표면
학 번: 2013-20656